D. SUPPLEMENTARY MATERIAL — PART D

VIBRATIONAL PREDISSOCIATION

Li^+–H_2 COMPLEX

TABLE DI: Vibrationally predissociating $v_r\, b\, k{=}0\, v_R\, J{=}0$ states of the Li^+–H_2 complex.
3D perturbative (CM)[a] versus 3D 'exact'[b] results for energies (E), total widths (Γ), and populations ($P_j{=}\Gamma_{vj}/\Gamma{\times}100\%$ and $P_v{=}\sum P_j$) of decay channels $H_2(v,j){+}Li^+$ with $v{=}v_r{-}1$. $\Delta E^{(0)}{=}E^{(0)}{-}E$, $\Delta E^{\rm CM}{=}E^{\rm CM}{-}E$, $\delta\Gamma{=}(\Gamma^{\rm CM}/\Gamma{-}1){\times}100\%$. Accuracy of results from the 2D-GR approach[c]: the deviations $\Delta E^{\rm 2D}{=}E^{2D}{-}E$ and $\delta\Gamma^{\rm 2D}{=}(\Gamma^{\rm DVGR}/\Gamma{-}1){\times}100\%$ listed in angle brackets.

v_r	b	v_R	$\Delta E^{(0)\,d}$	$\Delta E^{\rm CM}$	$\langle\Delta E^{\rm 2D}\rangle^d$	E^{de}	$\delta\Gamma$	$\langle\delta\Gamma^{\rm 2D}\rangle$	Γ^d	P_j, $P_j^{{\rm CM}f}$					P_v
										$j{=}0$	2	4	6	8	
1	0	0	-9.866^g	0.007	⟨ 8.247⟩	2378.491	1.5	⟨ 3.8⟩	2.37 (−2)	0.8	93.4	5.8			
										0.8	92.6	6.6			
		1	-8.767^g	0.009	⟨ 7.131⟩	2789.040	1.7	⟨ 5.0⟩	6.84 (−2)	0.8	87.7	8.0	3.6		
										0.8	86.3	10.1	2.8		
		2	-7.453^g	0.013	⟨ 5.860⟩	3142.481	3.0	⟨ 5.0⟩	1.12 (−1)	0.9	86.5	11.1	1.5		
										0.9	84.4	13.6	1.1		
		3	−6.035	0.018	⟨ 4.552⟩	3438.954	2.4	⟨ 3.9⟩	1.46 (−1)	1.0	83.7	11.6	3.7		
										1.0	81.7	15.8	1.5		
		4	−4.631	0.019	⟨ 3.334⟩	3679.296	4.9	⟨ 5.3⟩	1.54 (−1)	1.1	82.8	14.6	1.5		
										1.0	80.2	17.6	1.2		
		5	−3.324	0.018	⟨ 2.271⟩	3864.893	5.7	⟨ 5.2⟩	1.42 (−1)	1.1	82.2	15.1	1.6		
										1.1	79.5	18.1	1.3		
		6	−2.214	0.009	⟨ 1.417⟩	3998.446	12.5	⟨ 6.8⟩	1.11 (−1)	1.2	79.5	19.0	0.3		
										1.2	81.6	16.9	0.3		
		7	−1.292	0.010	⟨ 0.795⟩	4085.736	7.0	⟨ 4.9⟩	7.46 (−2)	1.3	81.6	15.8	0.2	1.1	
										1.2	79.2	17.9	0.4	1.3	
		8	−0.629	0.007	⟨ 0.378⟩	4134.417	7.6	⟨ 4.6⟩	3.86 (−2)	1.3	80.5	17.0	0.4	0.8	
										1.3	77.8	19.4	0.6	0.9	
		9	−0.197	0.004	⟨ 0.116⟩	4155.187	9.8	⟨ 4.0⟩	1.23 (−2)	1.3	80.2	17.4	0.4	0.7	
										1.3	77.3	20.0	0.6	0.8	
	2	0	−5.686	0.021	⟨ 2.194⟩	3473.264	7.4	⟨22.4⟩	1.59 (−2)	0.1	16.7	29.2	54.0		
										0.1	20.9	34.2	44.8		
		1	−5.222	0.029	⟨ 1.784⟩	3778.283	6.6	⟨13.1⟩	3.34 (−2)	0.1	13.3	39.4	47.2		
										0.1	17.3	46.0	36.6		
		2	−4.276	0.037	⟨ 1.157⟩	4033.246	11.1	⟨12.3⟩	5.48 (−2)	0.1	17.2	39.7	43.0		
										0.1	21.9	43.9	34.1		
2	0	0	-20.202^g	0.033	⟨ 6.739⟩	6197.852	0.6	⟨ 4.4⟩^{h}	1.09 (−1)	0.9	72.1	26.1			99.1
										1.0	74.7	23.4			99.1
		1	-18.161^g	0.036	⟨ 5.621⟩	6612.956	3.4	⟨ 1.6⟩	2.90 (−1)	1.0	78.0	18.0	1.9		98.9
										1.0	76.9	19.7	1.3		98.9
		2	-15.669^g	0.051	⟨ 4.452⟩	6973.285	5.5	⟨ 1.6⟩	4.69 (−1)	1.0	77.4	19.5	0.7		98.6
										1.1	75.3	21.7	0.7		98.8
		5	−7.556	0.072	⟨ 1.503⟩	7729.987	9.3	⟨ 1.6⟩	6.08 (−1)	1.1	74.1	22.3	0.6		98.1
										1.1	70.8	25.3	1.0		98.2
		6	−8.106	-0.751^i	⟨−0.535⟩	7883.568	59.0	⟨17.6⟩	2.69 (−1)	0.6	73.2	10.7	13.8		98.3
										1.0	92.9	0.5	3.8		98.2
		7	−3.239	0.049	⟨ 0.480⟩	7979.424	11.2	⟨ 1.7⟩	3.50 (−1)	1.2	72.7	23.3	0.7		97.9
										1.2	69.0	26.7	1.2		98.1
	2	0	−12.202	0.126	⟨−0.069⟩	7316.381	56.5	⟨19.4⟩	2.80 (−2)	0.1	40.1	37.7	20.9		98.8
										0.1	37.0	39.4	22.6		99.1
3	0	0	−30.327	0.087	⟨ 4.564⟩	9796.336	−3.8	⟨ 0.1⟩^{h}	3.82 (−1)	1.1	57.0	39.9			98.0
										1.3	66.4	30.4			98.1
		1	−27.568	0.088	⟨ 3.360⟩	10215.485	4.4	⟨−1.0⟩	8.92 (−1)	1.3	68.5	27.4			97.2
										1.3	69.6	26.4			97.3
		2	−24.096	0.114	⟨ 2.281⟩	10581.741	6.9	⟨−1.0⟩	1.40	1.3	71.1	23.3	0.7		96.4
										1.3	70.6	23.9	0.8		96.6
		3	−20.210	0.140	⟨ 1.361⟩	10895.417	8.6	⟨−0.8⟩	1.75	1.2	69.4	24.2	0.9		95.7
										1.3	68.0	25.5	1.2		96.0
	2	0	−19.339	0.286	⟨−3.178⟩	10936.335	64.8	⟨16.1⟩	1.05 (−1)	1.2	36.7	43.2	17.8		98.9
										0.9	32.9	42.4	22.7		98.9

TABLE DI: continued

									j=1	3	5	7	
1	1	0	−7.673	0.017	⟨ 3.743⟩	2983.914	15.5	⟨13.1⟩	1.67 (−2)	9.1	72.0	18.9	
										9.0	71.7	19.3	
		1	−6.732	0.022	⟨ 2.977⟩	3335.862	6.1	⟨11.2⟩	6.37 (−2)	9.3	72.3	9.8	8.6
										9.8	73.4	9.9	6.9
		2	−5.598	0.029	⟨ 2.161⟩	3633.935	9.3	⟨11.2⟩	1.01 (−1)	10.5	73.5	11.1	4.9
										10.8	72.7	12.4	4.1
		3[j]	−4.620	0.029	⟨ 1.881⟩	3870.882	5.5	⟨21.6⟩	7.32 (−2)	10.7	69.5	8.7	11.1
										10.7	66.8	13.8	8.7
		4	−3.091	0.032	⟨ 0.751⟩	4060.586	13.4	⟨12.0⟩	1.19 (−1)	11.8	71.5	13.7	3.0
										11.8	69.3	16.4	2.5
		5	−2.255	−0.040	⟨ 0.759⟩	4189.186	22.7	⟨ 2.9⟩	6.92 (−2)	11.4	65.7	19.1	3.8
										12.0	68.0	18.1	1.9
		6	−0.771	0.016	⟨ 0.102⟩	4255.017	17.4	⟨12.1⟩	3.99 (−2)	12.3	69.8	15.7	2.2
										12.3	67.6	18.2	1.9
	3	0[j]	−4.447	0.021	⟨ 1.930⟩	3882.051	17.3	⟨−0.8⟩	5.54 (−2)	10.8	68.7	17.4	3.1
										11.3	70.4	16.3	2.0
		1[j]	−4.294	0.103	⟨ 1.959⟩	4176.812	−9.7	⟨30.4⟩	3.90 (−2)	7.2	45.4	5.6	41.8
										5.8	36.0	20.4	37.8
2	1	0	−16.275	0.067	⟨ 1.002⟩	6813.442	21.4	⟨11.6⟩	1.08 (−1)	9.0	82.6	7.7	99.3
										9.4	86.1	3.6	99.1
3	1	0	−25.081	0.175	⟨−2.544⟩	10421.577	29.1	⟨11.9⟩	2.70 (−1)	8.8	68.6	20.5	97.9
										8.6	64.5	24.9	98.0

[a]From the implementation of the bound-continuum configuration-mixing theory[1] described in Sec. III of the paper. $E^{(0)}$ — the 0-th order approximation to the energy E is obtained as the energy of related state in the bound-state subspace Q which includes v-channels with v=v_r, v_r+1, v_r+2.

[b]From the life-time matrix[2] analysis, see Ref. 3.

[c]The approach originally proposed in Refs. 4 and 5, under the name 'diabatic vibrational golden rule' (DVGR) approximation, for studying van der Waals complexes of Cl_2 and ICl molecules with rare gas atoms. It differs from the 3D-CM approach in the following respects: (i) the Q- and P-subspaces are built of only one v-state of the diatomic subunit, v=v_r and v=v_r−1, respectively, (ii) only 0-th order approximation is used for energy of the predissociating state, i.e., E^{2D}=$E^{(0)}$, and (iii) the width is calculated according to the Golden Rule formula Γ^{2D}=$2\pi\langle \mathbf{F}_Q^B|\mathbf{H}_{QP}\,\mathbf{F}_P^{(+)}(E)\rangle\delta(E-E^{(0)})$, i.e. using the P-subspace function at E=$E^{(0)}$.

[d]Given in cm^{-1}. [e]The energy is relative to the $H_2(v{=}0, j{=}0)$+Li^+ dissociation limit.

[f]Listed in the lower line for each $v_r\,b\,v_R$ case.

[g]These deviations are counterparts of the shifts between energies listed in Table 2 of Ref. 6 in columns 'Quasibound state' and 'Resonance': −8.45, −6.82, −6.63 cm^{-1} for v=1 and −11.23, −9.59, −9.31 cm^{-1} for v=2. The latter shifts are nearly two times smaller than the $\Delta E^{(0)}$'s for v_r=2. This indicates that the PES used in Ref. 6 entails substantially stronger $r-(R,\theta)$ coupling than the PES used here. The same conclusion may be drawn from inspection of the widths from this PES (as assigned in Table IX), from their strong departure from v_r^2 scaling.

[h]The values of $\delta\Gamma^{2D}$ for v_r=2, 3 states might suggest that the 2D-GR approximation is much more accurate than the 3D-CM approach in describing these states. However, it should be realized that the 2D widths are approximations actually not to the 3D 'exact' widths but to widths obtainable with bases which include only two v-states, v=v_r−1 and v=v_r. Energies and widths from close-coupling calculations using such restricted bases differ from the fully convergent results the more substantially the higher the v_r is. In the case of the v_r=3 b=0 v_R=0 state, for example, the energy is higher by as much as 35.5 cm^{-1} and the width is smaller by 26%. Because of the big (and increasing with v_r) shift contributed to the level positions, the coupling of v=v_r with v=v_r+1 state has also a significant impact on the level widths. Therefore it is essential that this coupling be present in the Q-subspace. Thus, the good consistency of the 2D-GR widths with the exact results should be regarded as fortuitous. Similar conclusion was reached in Ref. 5 from tests of the DVGR approach on the Ne-ICI complex.

[i]This relatively large deviation is due to strong mixing between the states v_r=2 b=0 v_R=6 and v_r=2 b=2 v_R=2.

[j]Function of the state is shown and analyzed in Figs. D1c–d.

$Li^+–H_2$

Fig. D1. Vibrationally predissociating states v_r=1 b k v_R J p

D1a. Total widths of J=k levels (cf. Fig. 8)

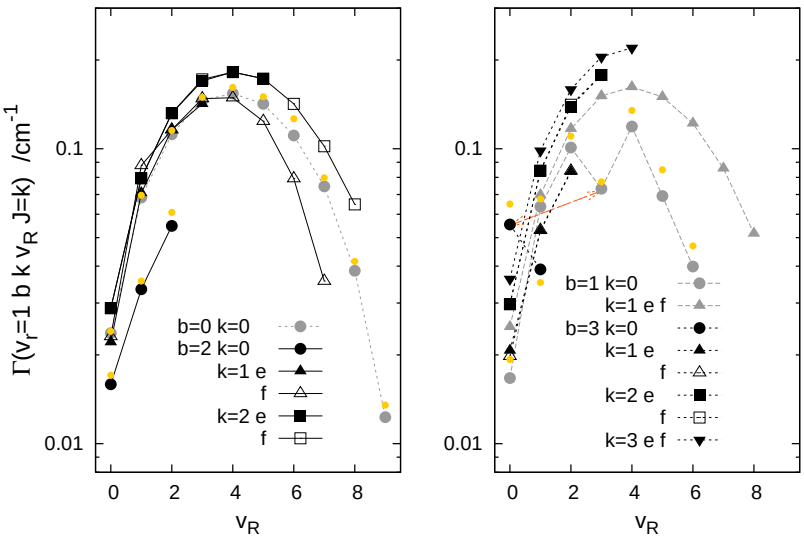

States formed with para- and ortho-H_2, are shown here in separate panels (and only those which can decay by pure vibrational predissociation, cf. Table BI in Ref. 7). It is better exposed that the widths of states with b–k>0 are smaller than the b=k widths for given values of b and v_R. The red arrow connects heavily mixed states. The mixing causes the dip in the b=1 k=0 curve, see part d of the figure. Results of the perturbative calculations for k=0 states (see Table DI) are shown here with the yellow symbols.

D1b. Populations (Γ_j/Γ) of decay channels $H_2(v$=0 $j)$ + Li^+ — correlations with the quantum numbers of the states (cf. Fig. 12)

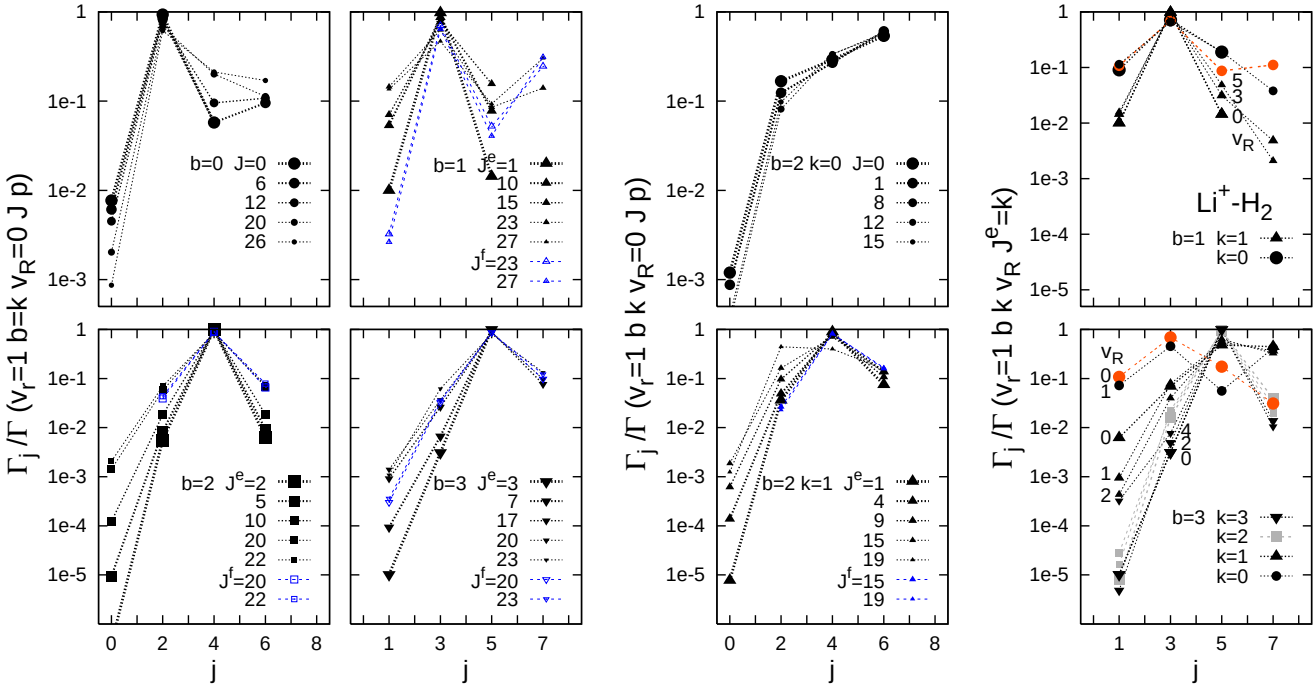

The left-hand panels concern states with v_θ=b–k=0. It is shown that the property of decay of these states — almost entirely to channels with j=b+2 — weakens with growing J. The right-hand and middle panels provide further examples of the fact that the population of decay channels changes substantially with excitation of bending vibrations in the complex — the peak population shifts towards the energetically highest channel. Orange symbols mark cases of departure from this tendency.

D1c. Functions of the states $\Psi^{(+)}(E_{\rm res}, R, \theta)$

approximated by bound state functions in the entire (P+Q) space

Probability densities $\rho(\theta, R)$

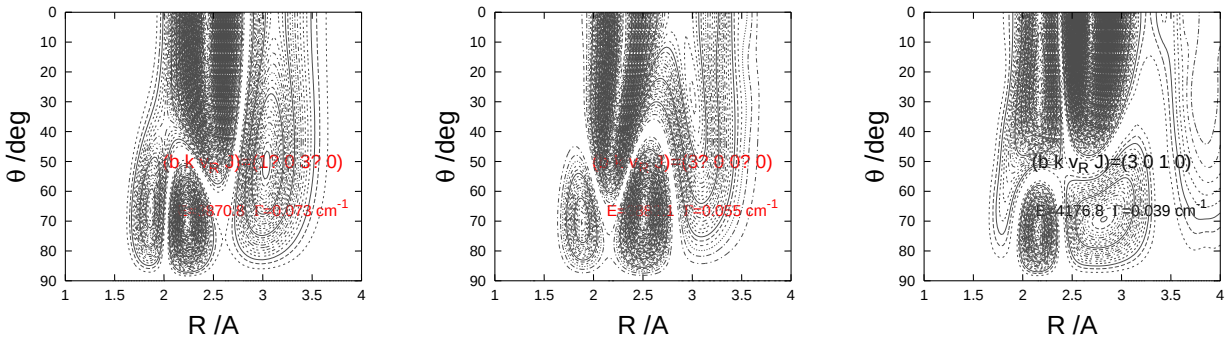

Shown are the two cases marked with orange symbols in part b of the figure and one 'regular' case (in the rightmost panel).

D1d. Natural expansion analysis (NEA)*

of related bound states functions in the Q-subspace

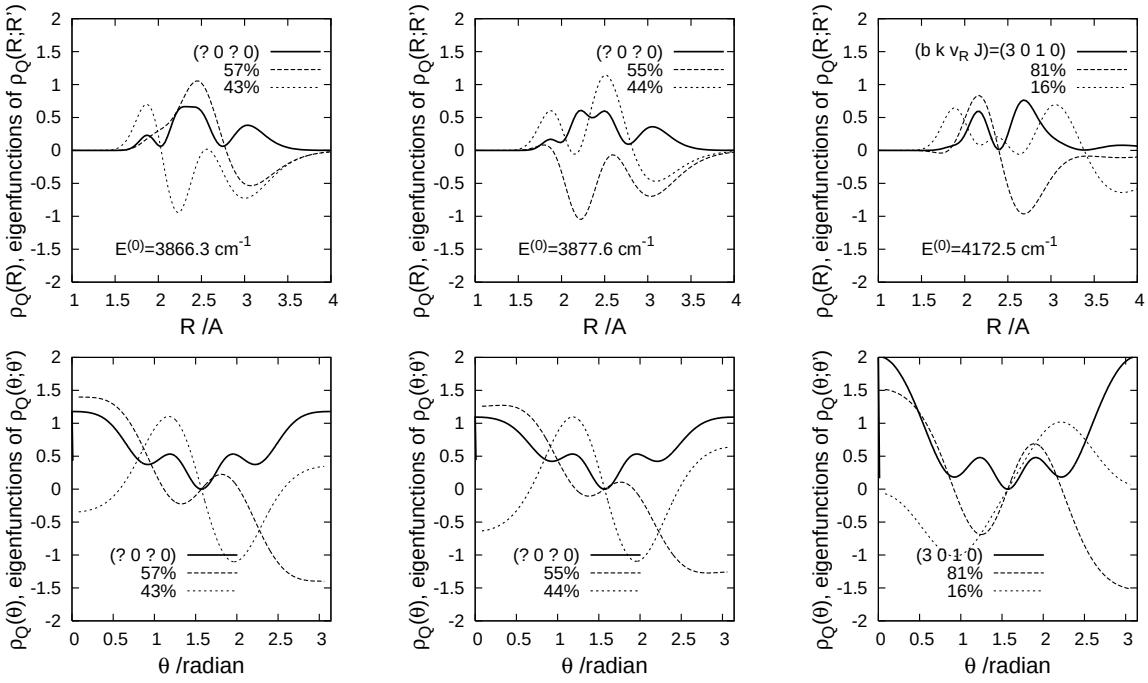

* details of NEA are as described in Ref. 8.

Here plotted are: the diagonal elements of the density kernels, $\rho(R,R){:=}\rho(R)$ and $\rho(\theta,\theta){:=}\rho(\theta)$, and two their most occupied eigenfuctions (the natural orbitals). The occupancies are listed in the legend of each panel.

The state (3 0 1 0) represents a regular case in the sense that its assignment is well justified by the shape of the function: i) by the high occupancy of the leading natural orbitals in the R- and θ-coordinates (81%), and ii) by the clear structure of both these orbitals (the number of zeros in them).

D1e. Accuracy of energies and widths of v_r=1 b=k v_R=0 J p states determined within the 3D-CM and 2D approaches

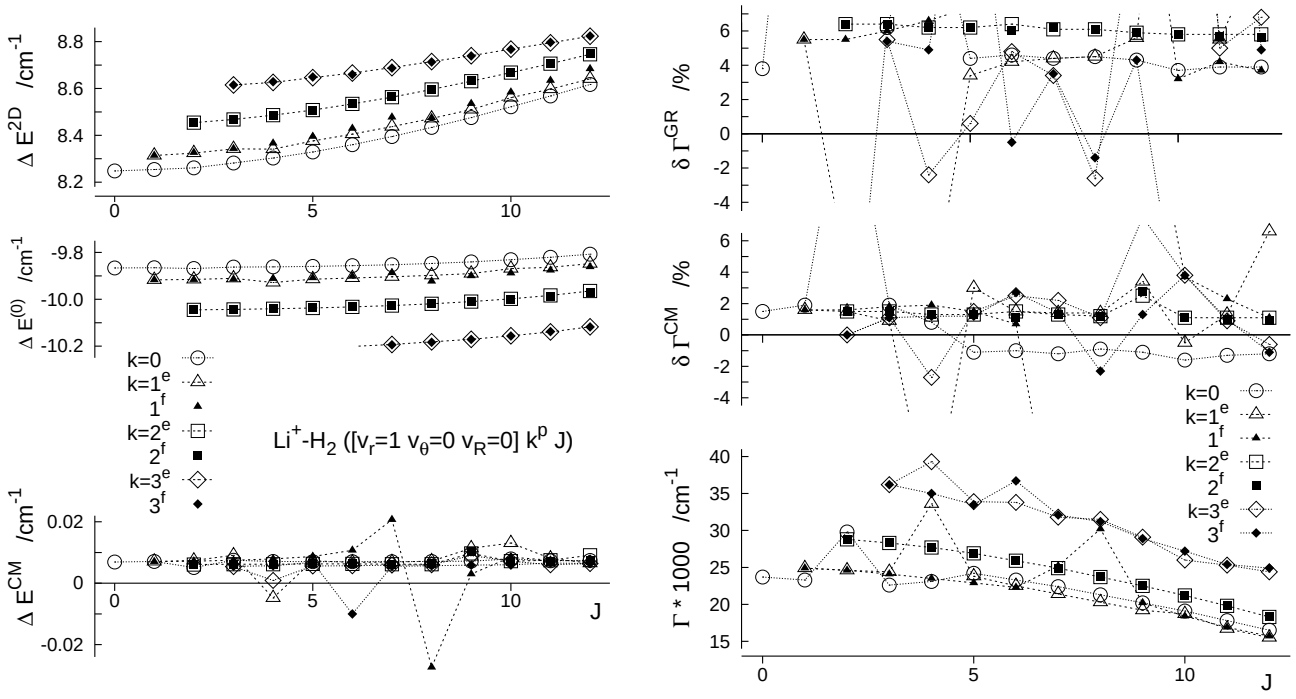

The plotted deviations ΔE^{2D}, $\Delta E^{(0)}$, ΔE^{CM}, $\delta\Gamma^{GR}$, and $\delta\Gamma^{CM}$ from 3D 'exact' energies E and widths Γ of the states are defined in the caption of Table DI. The 'exact' values of E and Γ can be found in Table BIV of Ref. 7. The Γ's are also plotted here in the bottom right panel (enlarged view of a fragment of Fig. 9 of the paper).

COMMENTS

The error ΔE^{CM} is approximately the same for the different rotational states (J, k) within the selected vibrational state, $[v_r\, v_\theta\, v_R]$=[1 0 0]. The error ΔE^{2D} does not have the property; it is clearly larger for k=2, 3 than for k=0, 1 and grows with increasing J.

In Fig. B3 of Part B, it is shown that the rate of growth of the error ΔE^{2D} with the number J and the dependence on k vary between different vibrational states. This lowers, of course, the suitability of the 2D approximation to simulations of absorption spectra.

In view of the large disproportion in the size of errors of the energies of the states, ΔE^{CM} and ΔE^{2D}, the errors of the widths, $\delta\Gamma^{CM}$ and $\delta\Gamma^{2D}$ (2D:=GR, see Table D1), differ little. Generally, in cases of well isolated predissociating states the accuracy of the widths determined with the Golden Rule formula is rather weakly correlated with accuracy of the energies of the states. Quite different is, of course, the situation when some disturbances (mixing) between the states occur. The relative errors of the widths become then high. Such disturbances are not rare in the Li^+-H_2 complex. Therefore, if accuracy of the widths is of concern relaying on the perturbative approach (on the isolated resonance version of it) is not quite safe. A checking tool, like the 3D exact life-time matrix approach, should be at hand.

Li^+–D_2 COMPLEX

TABLE DII: Vibrationally predissociating $v_r\, b\, k{=}0\, v_R\, J{=}0$ states of the Li^+–D_2 complex. Perturbative (CM)[a] versus 'exact' (LT)[b] results for energies (E), total widths (Γ), and populations ($P_j{=}\Gamma_{vj}/\Gamma{\times}100\%$ and $P_v{=}\sum P_j$) of decay channels $D_2(v,j)$+Li^+ with $v{=}v_r{-}1$. $\Delta E^{(0)}{=}E^{(0)}{-}E$, $\Delta E^{\rm CM}{=}E^{\rm CM}{-}E$, $\delta\Gamma{=}(\Gamma^{\rm CM}/\Gamma{-}1){\times}100\%$. Accuracy of results from the 2D approach: the deviations $\Delta E^{\rm 2D}{=}E^{2D}{-}E$ and listed in angle brackets.

v_r	b	v_R	$\Delta E^{(0)\,c}$	$\Delta E^{\rm CM}$	$\langle\Delta E^{\rm 2D}\rangle^c$	$E^{c\,d}$	$\delta\Gamma$	Γ^c	P_j, $P_j^{\rm CM\,e}$					P_v
									$j{=}0$	2	4	6	8	
1	0	0	−9.896	0.010	⟨ 9.391⟩	1131.835	29.4	8.29 (−3)	0.6	97.9	1.5			
									0.7	97.5	1.8			
		1	−9.051	0.007	⟨ 8.506⟩	1467.733	−2.3	2.52 (−2)	0.5	79.6	18.8	1.1		
									0.5	81.2	17.4	0.9		
		2	−8.059	0.009	⟨ 7.481⟩	1767.906	−1.1	4.55 (−2)	0.3	80.6	17.3	1.8		
									0.4	81.0	17.1	1.5		
		3	−6.974	0.012	⟨ 6.381⟩	2032.430	0.0	6.41 (−2)	0.2	80.7	18.4	0.7		
									0.3	80.7	18.3	0.7		
		4	−5.818	0.014	⟨ 5.037⟩	2262.003	0.6	6.91 (−2)	0.1	93.5	6.0	0.1	0.3	
									0.1	93.6	5.8	0.2	0.3	
		5	−4.760	0.017	⟨ 4.209⟩	2455.465	1.5	8.38 (−2)	0.1	78.4	20.1	1.3	0.1	
									0.1	77.5	20.8	1.5	0.1	
		6	−3.718	0.017	⟨ 3.223⟩	2615.390	2.0	8.20 (−2)	0.0	79.7	19.1	1.2	0.0	
									0.0	78.8	19.8	1.4	0.0	
		7	−2.779	0.015	⟨ 2.358⟩	2742.526	1.3	7.41 (−2)	0.0	81.2	17.7	1.1	0.0	
									0.0	80.4	18.4	1.2	0.0	
		8	−2.020	0.050	⟨ 1.659⟩	2838.899	2.0	5.95 (−2)	0.0	73.9	23.9	2.0	0.2	
									0.0	69.4	26.7	3.5	0.4	
		9	−1.315	0.010	⟨ 1.075⟩	2907.935	3.3	4.39 (−2)	0.0	80.7	18.1	1.2	0.0	
									0.0	79.8	18.9	1.3	0.0	
		10	−0.802	0.008	⟨ 0.649⟩	2953.334	3.9	2.85 (−2)	0.0	78.1	20.3	1.5	0.1	
									0.0	76.8	21.3	1.8	0.1	
		11	−0.424	0.007	⟨ 0.338⟩	2979.770	5.2	1.55 (−2)	0.0	72.7	24.7	2.5	0.1	
									0.0	68.8	27.5	3.5	0.2	
		12	−0.236	−0.065	⟨−0.195⟩	2992.044[f]	−54.9	1.45 (−2)	0.2	71.2	11.2	15.4	2.0	
									0.1	95.7	2.9	1.2	0.1	
	2	0	−6.586	0.016	⟨ 3.841⟩	1990.399	14.7	5.86 (−3)	0.0	10.9	61.5	27.6		
									0.0	10.8	58.6	30.6		
		1	−5.902	0.020	⟨ 3.474⟩	2258.352	6.6	3.15 (−2)	0.1	5.2	77.3	10.6	6.8	
									0.1	5.0	74.4	15.5	5.0	
		2	−5.074	0.024	⟨ 2.610⟩	2494.417	12.0	4.14 (−2)	0.1	20.3	55.8	16.6	7.2	
									0.1	20.1	51.0	23.4	5.4	
		3	−4.194	0.028	⟨ 1.967⟩	2696.302	14.4	5.74 (−2)	0.1	16.5	55.6	22.7	5.1	
									0.1	16.3	49.9	30.7	3.0	
		4	−3.304	0.023	⟨ 1.466⟩	2864.419	14.9	5.81 (−2)	0.2	20.5	53.6	24.3	1.4	
									0.2	20.5	49.2	26.6	3.5	
		5	−2.338	0.098	⟨ 0.619⟩	2991.230[f]	35.3	5.58 (−2)	0.2	9.7	56.6	30.3	3.2	
									0.2	16.3	46.7	34.3	2.5	
	4	0	−4.303	0.012	⟨ 2.744⟩	2607.876	−2.7	1.85 (−3)	0.0	1.6	23.3	13.5	61.6	
									0.0	1.6	20.4	28.4	49.6	
2	0	0	−20.161	0.038	⟨ 8.866⟩	3926.603	−9.3	3.24 (−2)	0.8	69.2	29.5			99.5
									1.1	77.0	21.6			99.7
		1	−18.534	0.033	⟨ 7.971⟩	4264.951	−5.0	8.94 (−2)	0.9	74.2	22.1	2.2		99.4
									1.1	77.8	19.4	1.2		99.5
		2	−16.614	0.037	⟨ 6.966⟩	4568.653	−2.3	1.56 (−1)	0.9	75.6	21.6	1.2		99.3
									1.0	77.4	19.9	1.0		99.3
	2	0	−13.905	0.069	⟨ 2.227⟩	4796.029	23.9	2.25 (−2)	0.0	8.1	44.6	46.8		99.5
									0.0	8.2	42.0	49.3		99.5

TABLE DII: continued

3	0	0	−30.331	0.091	⟨ 7.947⟩	6606.877	−11.9	8.54 (−2)	0.9	67.5	30.6			99.1
									1.1	77.9	20.1			99.1
		1	−28.011	0.079	⟨ 7.029⟩	6947.438	−6.1	2.26 (−1)	1.4	70.9	26.4			98.7
									1.7	76.3	20.8			98.8
		2	−25.256	0.089	⟨ 6.049⟩	7254.304	−3.2	3.89 (−1)	1.4	73.5	20.9	2.5		98.3
									1.8	76.3	18.4	1.8		98.3
	2	0	−21.637	0.149	⟨ 0.094⟩	7486.494	30.4	8.64 (−2)	0.1	12.1	86.6	0.3		99.1
									0.1	11.7	78.0	9.2		99.0
									j=1	3	5	7	9	
1	1	0	−8.090	0.012	⟨ 5.877⟩	1587.460	4.9	9.00 (−3)	3.3	76.8	19.9			
									3.3	76.8	19.9			
		1	−7.366	0.013	⟨ 5.196⟩	1891.797	−4.2	3.56 (−2)	2.9	69.2	12.7	15.2		
									3.2	69.9	17.6	9.3		
		2	−6.481	0.015	⟨ 4.392⟩	2160.775	5.4	5.55 (−2)	4.1	70.4	22.8	2.7		
									4.0	68.4	25.5	2.1		
		3	−5.491	0.019	⟨ 3.542⟩	2394.238	6.4	7.95 (−2)	4.5	68.1	24.0	3.4		
									4.5	65.5	27.0	3.0		
		4	−4.459	0.020	⟨ 2.694⟩	2592.111	7.7	9.25 (−2)	5.2	67.9	25.3	1.6		
									5.1	65.6	27.6	1.6		
		5	−3.491	0.024	⟨ 1.973⟩	2752.581	8.4	9.57 (−2)	5.1	61.2	30.1	3.3	0.3	
									5.0	57.1	34.0	3.7	0.3	
		6	−2.503	0.021	⟨ 1.305⟩	2878.409	9.2	8.73 (−2)	5.7	63.7	28.1	2.3	0.2	
									5.6	60.4	31.2	2.6	0.2	
		7	−1.659	0.012	⟨ 0.783⟩	2968.628	10.1	6.48 (−2)	6.4	69.8	22.5	1.0	0.3	
									6.3	67.6	24.6	1.3	0.2	
		8	−0.867	0.012	⟨ 0.393⟩	3023.581	11.0	3.87 (−2)	6.2	63.5	28.1	2.0	0.2	
									6.0	60.3	31.1	2.5	0.1	
		9	−0.259	0.007	⟨ 0.113⟩	3048.223	14.2	1.19 (−2)	6.2	61.9	29.4	2.3	0.2	
									5.9	58.5	32.7	2.8	0.1	
	3	0	−5.160	0.018	⟨ 2.844⟩	2327.928	−1.9	5.04 (−3)	0.2	17.8	47.7	34.3		
									0.3	20.9	51.0	27.8		
		1	−4.799	0.020	⟨ 2.501⟩	2564.936	11.0	1.25 (−2)	0.0	12.8	48.9	38.3		
									0.0	11.6	49.6	38.8		
		2	−4.056	0.026	⟨ 1.945⟩	2775.440	14.7	2.45 (−2)	1.9	42.0	27.0	18.2	10.9	
									2.0	46.1	21.8	21.1	9.0	
		3	−3.381	0.032	⟨ 1.489⟩	2953.181	18.9	3.32 (−2)	0.0	14.0	49.9	27.1	9.0	
									0.1	14.6	46.8	31.0	7.5	
	5	0	−4.617	0.014	⟨ 3.356⟩	2887.202	−5.8	4.29 (−3)	0.4	14.2	20.5	0.7	64.2	
									0.6	19.3	19.6	5.1	55.4	
2	1	0	−16.780	0.047	⟨ 4.491⟩	4386.468	−11.8	5.18 (−2)	2.0	62.8	34.9			99.7
									2.4	59.5	37.7			99.6
3	1	0	−25.626	0.120	⟨ 2.632⟩	7071.024	14.9	8.71 (−2)	3.6	79.7	15.5			98.8
									3.6	84.8	10.6			99.0

[a]The bound-continuum configuration-mixing theory[1] in its isolated-resonance version, implemented as described in Sec. III of the paper. [b]The life-time matrix analysis[2,3]. [c]Given in cm^{-1}.
[d]The energy is relative to the $D_2(v{=}0, j{=}0)$+Li^+ dissociation limit. [e]Listed in lower lines.
[f]Case of strong mixing; could be better described with the overlapping-resonance version of the CM theory.

COMMENT

The accuracy of the energies from the 3D-CM approach is really good, especially in view of the fact that the shifts from the 0-th order values are so big. The accuracy of the widths is much worse; these quantities are more sensitive to disturbances by nearby levels. Still, the values of $\Gamma^{\rm CM}$ and $P_j^{\rm CM}$ reasonably reflect the correlations of the 'exact' total and partial widths with the quantum numbers of the states. So, formulas of the 3D-CM approach may be exploited for a rationalization of the trends in the predissociation dynamics.

Detailed

BOUND-CONTINUUM CONFIGURATION MIXING ANALYSIS

of

v_r=1 b k v_R J=0 states

P-subspace — spanned by 7 basis functions: v=0 j=0, 2, . . . , 12 or v=0 j=1, 3, . . . , 13

Q-subspace — spanned by 21 diabatic basis functions with v=1−3 and j∈[0, 13]

Fig. D3. Interaction in the Q-subspace: $\langle 1|V_{\rm int}(r,R,\theta)|1\rangle_r + \varepsilon_{v=1}$

in the P-subspace: $\langle 0|V_{\rm int}(r,R,\theta)|0\rangle_r$

$P-Q$ coupling: $\langle 0|V_{\rm int}(r,R,\theta)|1\rangle_r$

$V_{\rm int}(r,R,\theta) = V(r,R,\theta) - \lim_{R\to\infty} V(r,R,\theta)$ — the interaction potential

$\langle v|V_{\rm int}(r,R,\theta)|v'\rangle_r$ — matrix elements between vibrational functions of D_2

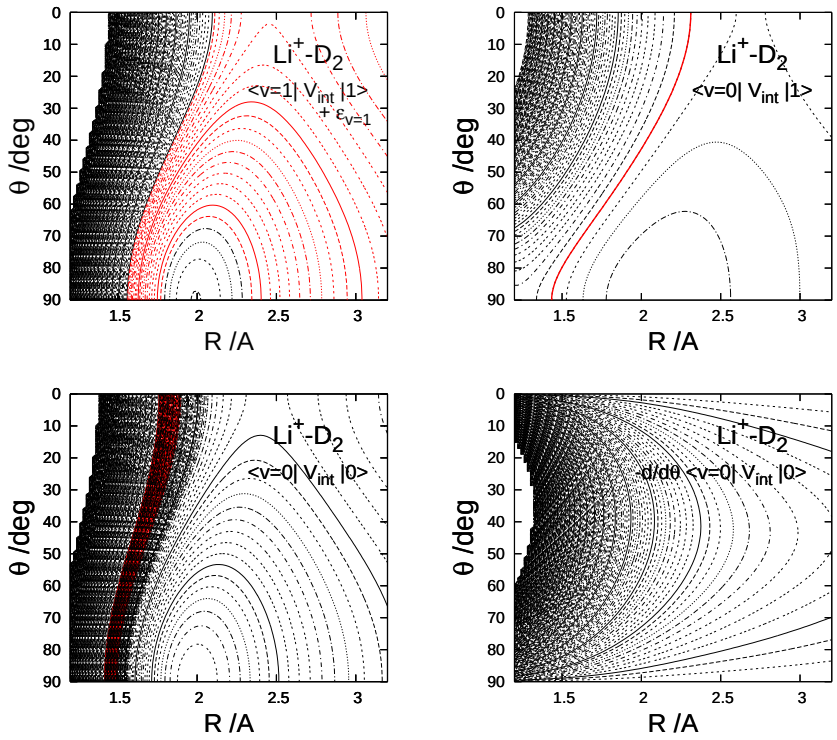

The red contours in the upper left panel show the region of bound states in the Q-subspace, 1132≤E<ε_{10}=2993 cm^{-1}. The corresponding energy region on the interaction potential surface in the P-subspace is indicated by the red strip in the bottom left panel. The dark parts in the two panels are the repulsive walls above the ε_{10}- and the ε_{00}- thresholds, respectively. The contours within the wells are drawn with step of 100 cm^{-1}. In the upper right panel, the contours are drawn in step of 50 cm^{-1} starting from -150 cm^{-1}. The 0 contour is shown in red. In the bottom right panel, the torque in the P-subspace is shown, $\frac{\partial}{\partial\theta} < V_{\rm int} > (R,\theta)$. It is 0 at θ=0,π/2, and π.

Fig. D4. Bound states functions in the Q-subspace: $\Psi_{\rm Q}$

Probability densities: $\rho_Q = \Psi_{\rm Q}\,\Psi^*_{\rm Q}$

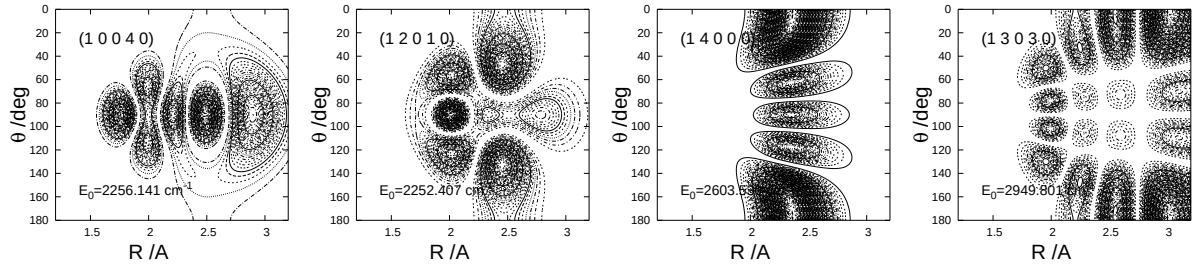

Fig. D5. Perturbed functions in the P-subspace:
$\Phi_P^{(+)}(E) = [E^{(+)} - H_{PP}]^{-1} H_{PQ}\,\Psi_Q$

at $E = E_0 (:= E^{(0)})$

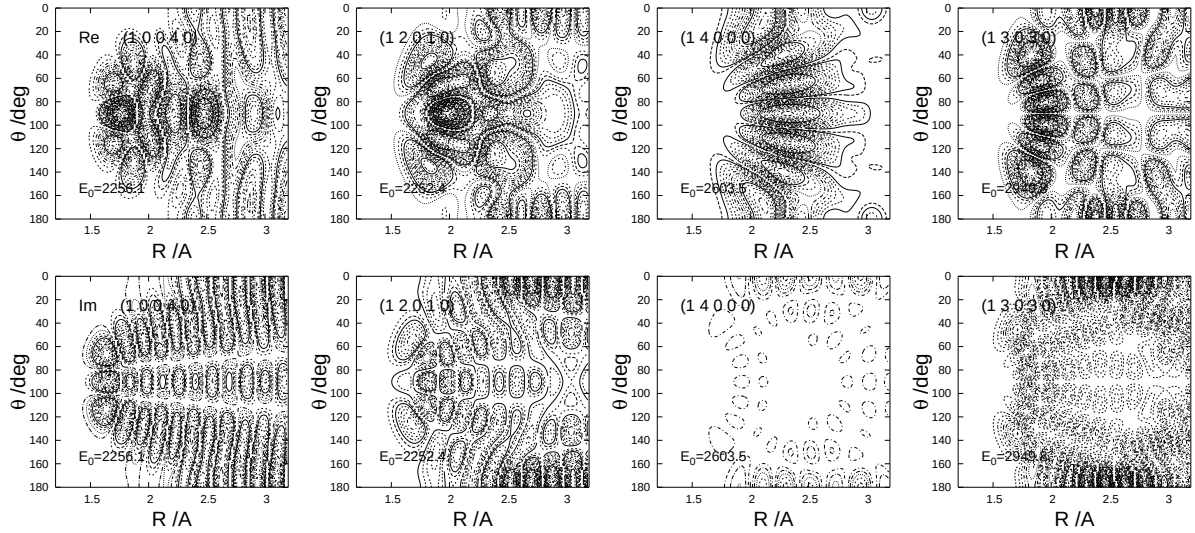

D6. Level shifts $E^{\rm shft}$ and total widths Γ as functions of R- and θ-coordinates

$$E^{\rm shft} = {\rm Re}\,\Psi_Q\,H_{QP}\,\Phi_P^{(+)}\,, \qquad \Gamma = -2\,{\rm Im}\,\Psi_Q\,H_{QP}\,\Phi_P^{(+)}$$

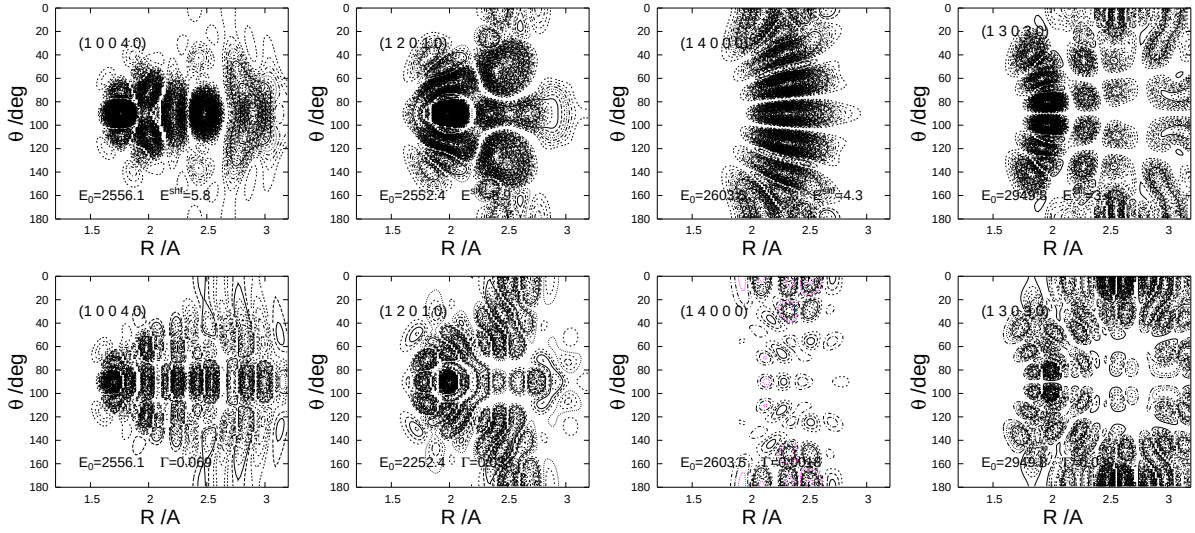

Fig. D7. Partial widths for decay into $D_2(v{=}0\,j)$ + Li^+ channels as functions of R- and θ- coordinates

$$\Gamma_j(R,\theta) = \gamma_j(R,\theta)\times\gamma_j^*$$

$$\gamma_j = \sqrt{2\pi}\,\Psi_Q\,H_{QP}\,\Psi_P^{(+)}(E{=}E_0, j)$$

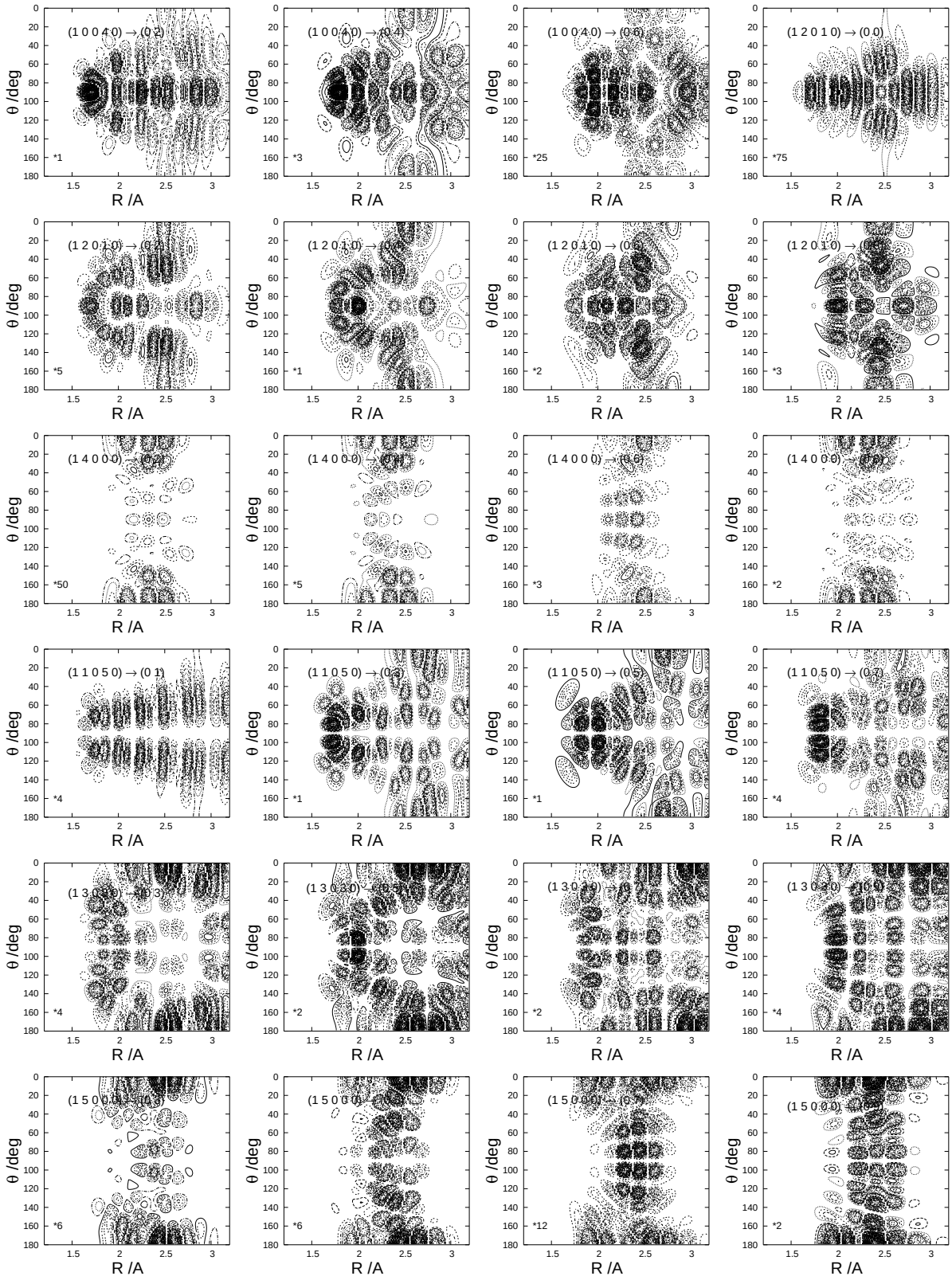

In left lower corner of each panel listed is the factor by which the shown function $\Gamma_j(R,\theta)$ is multiplied. The relative magnitudes of the functions $\Gamma_j(R,\theta)$ that pertain to the same state $(v_r\,b\,k\,v_R\,J)$ are approximately described by ratios of these factors. The functions $\Gamma_j(R,\theta)$ with the smallest factors determine the shapes of the total width functions $\Gamma(R,\theta)$ of the states; compare with Fig. D6 (panels in the lower row).

Fig. D4a. Perturbing functions: $\Psi_Q H_{QP}$

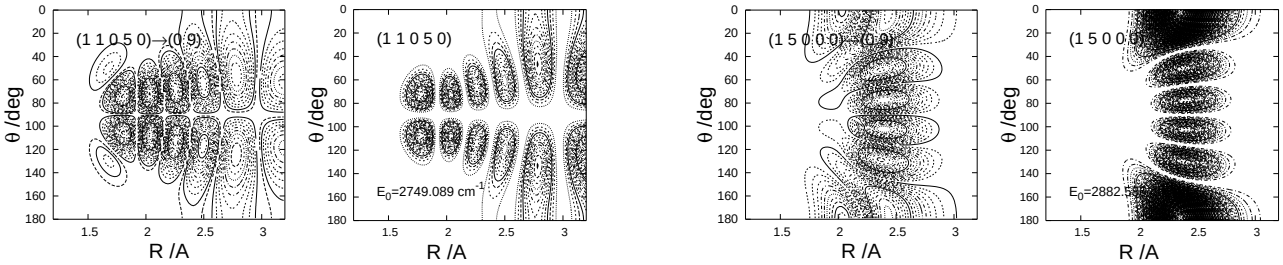

For two predissociating states, with v_θ=$b-k$=1 and 5, shown are the functions $\Psi_Q V^{QP}_{j'}(R,\theta)$ with j'=9, defined in Eq. (D7). For comparison with the structures of Ψ_Q, plots of the probability densities $\rho_Q(E_0;R,\theta)$ are added (in the second and forth panel from the left), cf. Eq. (D1).

Fig. D8. Scattering functions of $D_2(v{=}0\,j)$ + Li^+ in the P-subspace $\Psi^{(+)}_P(E,j)$

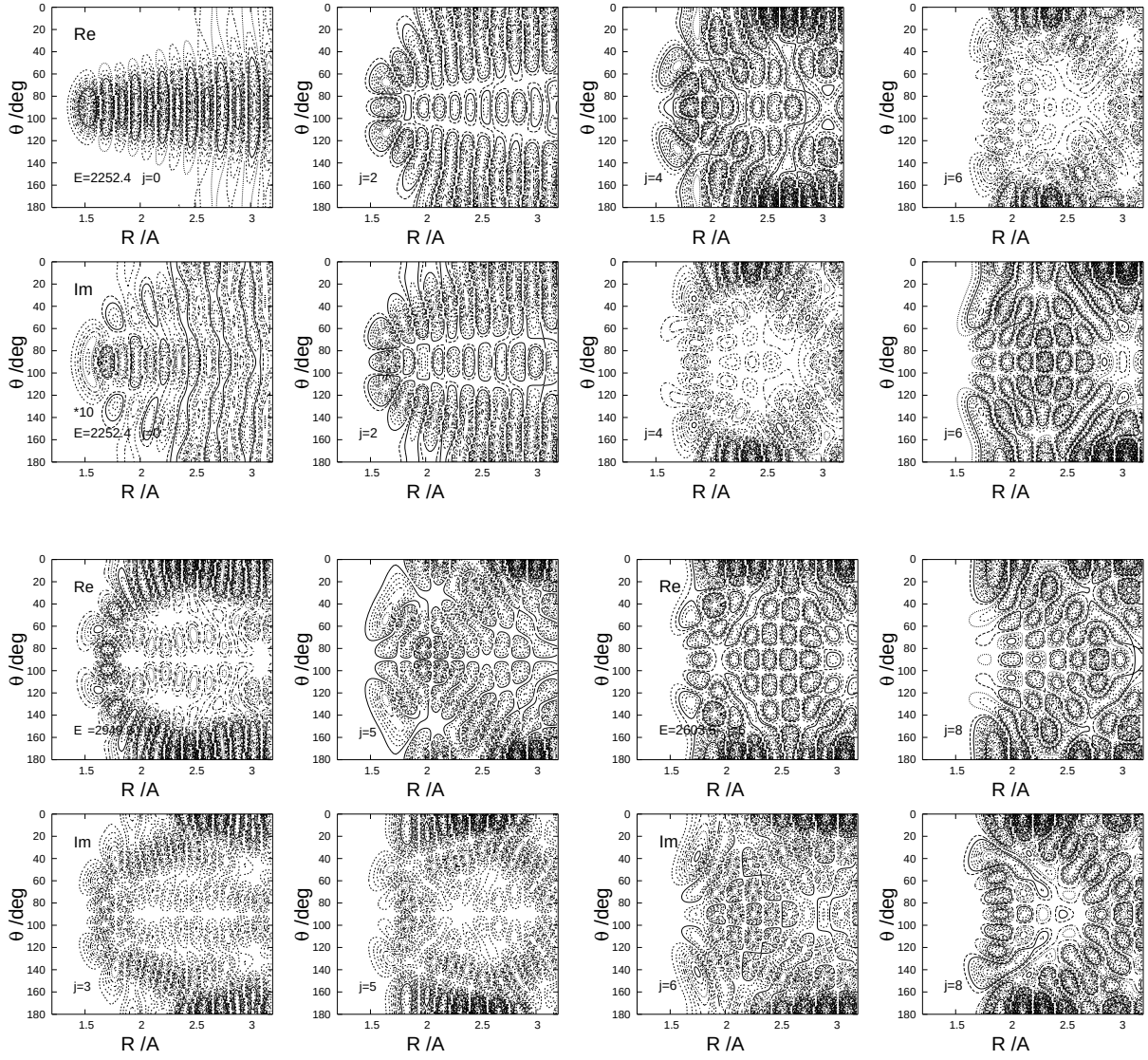

The functions are shown at three energies E, 2252.4, 2949.8, and 2603.6 cm^{-1}, equal to energies E_0 of (1 2 0 1 0), (1 3 0 3 0), and (1 4 0 0 0) states, respectively. At the first energy, the functions of all open channels j are shown in the upper two rows (Im-part below Re-part). Functions of two highest channels are shown only at the other E's.

The functions plotted in Figs. D4–D8 are:

$$\rho_Q(E_0;R,\theta) \;=\; \sum_{vj\in Q}\sum_{\tilde v\tilde j\in Q} F^Q_{vj}(E_0;R)\,\tau_j(\theta)\,\langle vj|\tilde v\tilde j\rangle_r\,\tau_{\tilde j}(\theta)\,F^Q_{\tilde v\tilde j}(E_0;R)\,, \tag{D1}$$

$$\Phi^{(+)}_P(E;R,\theta) \;=\; \sum_{j'\in P} f^{P(+)}_{j'}(E;R)\,\tau_{j'}(\theta)\,, \tag{D2}$$

$$\Psi^{(+)}_P(E,j;R,\theta) \;=\; \sum_{j'\in P} F^{P(+)}_{j'}(E,j;R)\,\tau_{j'}(\theta)\,, \tag{D3}$$

$$E^{\rm shft}(R,\theta) \;=\; {\rm Re}\sum_{j'\in P}\Psi_Q V^{QP}_{j'}(R,\theta)\,f^{P(+)}_{j'}(E{=}E_0;R)\,, \tag{D4}$$

$$\Gamma(R,\theta) \;=\; -2\,{\rm Im}\sum_{j'\in P}\Psi_Q V^{QP}_{j'}(R,\theta)\,f^{P(+)}_{j'}(E{=}E_0;R)\,, \tag{D5}$$

$$\gamma_j(R,\theta) \;=\; \sqrt{2\pi}\sum_{j'\in P}\Psi_Q V^{QP}_{j'}(R,\theta)\,F^{P(+)}_{j'}(E{=}E_0,j;R) \tag{D6}$$

where

$$\Psi_Q V^{QP}_{j'}(R,\theta) \;:=\; \sum_{vj\in Q} F^Q_{vj}(E_0;R)\,\tau_j(\theta)\sum_L\langle vj|V_L(R,r)|0j'\rangle_r\,P_L(\cos\theta)\,\tau_{j'}(\theta)\,, \tag{D7}$$

$$\tau_j(\theta) \;=\; (-1)^j\sqrt{j{+}\tfrac12}\,P_j(\cos\theta)\,, \tag{D8}$$

E_0 is the energy of the bound state in the Q-subspace related to the predissociating $(v_r\,b\,k\,v_R\,J)$ state shown in a given panel. [It is the 0-th order approximation to the energy E of the state which is denoted as $E^{(0)}$ in Table DII]. The symbol γ_j which stands in the definitions of the coordinate-dependent widths without arguments is indeed the integrated decay amplitude

$$\int\gamma_j(R,\theta)\,dR = \int\gamma_j(\theta)\,\sin\theta\,d\theta \;=\gamma_j\,.$$

The radial functions $F^{P(+)}_{j'}(E,j;R)$, $f^{P(+)}_{j'}(E;R)$, and $F^Q_{vj}(E_0;R)$ are presented in Figs. D9–D10.

COMMENT

Inspecting Figs. D5, D4, and D8 one notices that:
(i) the structures of the real and imaginary parts of the perturbed functions $\Phi^{P(+)}$ are rather different,
(ii) the functions Re $\Phi^{P(+)}$ resemble the respective bound state functions Ψ_Q in the Q-subspace, i.e. the constituents of the perturbing functions $H_{PQ}\Psi_Q$,
(iii) the structures of Im $\Phi^{P(+)}$ for $(1\,b\,0\,v_R\,0)$ states with $b{<}4$ are similar to the structures of the scattering functions $\Psi^{P(+)}(E,j)$ for $E{=}E_0{\approx}E_{\rm res}$ and $j{=}b{+}2$.
These observations can easily be explained using the spectral representation of the Green operator $[E^{(+)}{-}H_{PP}]^{-1}$. Namely, different states of H_{PP} dominate in forming the Re- and Im-parts of $\Phi^{P(+)}$. Bound states, most likely $(v_r{=}0\,b\,v_R\,0)$, contribute to the Re-part and scattering states of energy E to the Im-part. Precisely, the relation of this part to the scattering states is the following, see Eq. (D17):

$${\rm Im}\,\Phi^{(+)}_P(E;R,\theta) = -\sqrt{\frac{\pi}{2}}\sum_j\Psi^{(+)}_P(E,j;R,\theta)\,\gamma^*_j := -\sqrt{\frac{\pi}{2}}\Psi^{\rm tot}(E;R,\theta)\,.$$

The $\Psi^{\rm tot}$ appearing here is a counterpart of the total dissociation wavefunction which was used for visualization of photodissociation dynamics, Ref. 10. [The γ_j's replace, of course, the partial photodissociation amplitudes].

Fig. D9. Radial components of the functions $\Psi_P^{(+)}(E,j;R,\theta)$ in the diabatic and adiabatic bending representations $F_{j'}^{P(+)}(E,j;R)$ and $F_{j'_a}^{P(+)}(E,j;R)$

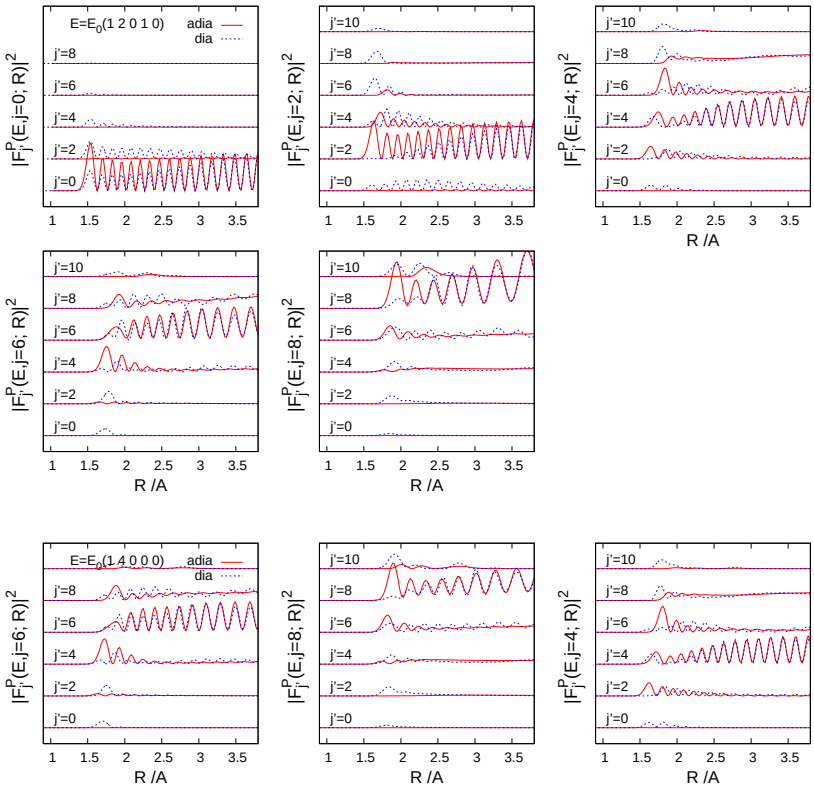

The adiabatic representation is defined separately for the Q- and P- subspace. The functions transformed to these representations, plotted or exploited in Figs. D9 – D11, are:

$$F_{j'_a}^{P(+)}(E,j;R) \;=\; \sum_{j'\in P} T^P_{j'j'_a}(R)\, F_{j'}^{P(+)}(E,j;R)\,, \tag{D9}$$

$$f_{j'_a}^{P(+)}(E;R) \;=\; \sum_{j'\in P} T^P_{j'j'_a}(R)\, f_{j'}^{P(+)}(E;R)\,, \tag{D10}$$

$$F^Q V_{j'_a}^{QP}(E_0;R) \;=\; \sum_{j'\in P} F^Q V_{j'}^{QP}(E_0;R)\, T^P_{j'j'_a}(R)\,, \tag{D11}$$

$$F_{j_a}^{Q}(E_0;R) \;=\; \sum_{vj\in Q} T^Q_{vj,v_a=1\,j_a}(R)\, F_{vj}^{Q}(E_0;R)\,, \tag{D12}$$

where $\mathbf{T}^P(R)\!:=\!\{T^P_{j'j'_a}(R)\}$ and $\mathbf{T}^Q(R)\!:=\!\{T^Q_{vj,v_aj_a}(R)\}$ are the orthogonal transformations which diagonalize the coupling matrices of the Hamiltonian H_{PP} and H_{QQ} in the diabatic representation,

$$\mathbf{H}^{ss}(R)\!=\!\mathbf{I}^s\frac{d^2}{dR^2}\!+\!\mathbf{W}^s\,,$$

i.e. the matrices $\mathbf{W}^s$:=$\{W^{J=0}_{vj,\tilde{v}\tilde{j}};\, vj,\, \tilde{v}\tilde{j}{\in}s\}$ for $s{=}P$ and $s{=}Q$, respectively, whose elements are

$$W^{J=0}_{vj,\tilde{v}\tilde{j}} = \delta_{vj,\tilde{v}\tilde{j}}\big[\varepsilon_{vj} + \frac{\hbar^2}{2\mu}\frac{j(j{+}1)}{R^2}\big] + \sum_L \langle vj|V_L(R,r)|\tilde{v}\tilde{j}\rangle_r\, g^L_{j\tilde{j}} \tag{D13}$$

with

$$g^L_{j\tilde{j}}{=}(-1)^{j+\tilde{j}}\frac{\sqrt{(2j{+}1)(2\tilde{j}{+}1)}}{2}\begin{pmatrix} j & L & \tilde{j}\\ 0 & 0 & 0\end{pmatrix}^2 .$$

The resulting adiabatic potentials are denoted as $e^s_{v_a\, j_a}(R)$, see Fig. D14.

Obviously, the symbol $F^Q V^{QP}_{j'}(E_0;R)$ denotes

$$F^Q V^{QP}_{j'}(E_0;R) = \sum_{vj\in Q} F^Q_{vj}(E_0;R)\sum_L \langle vj|V_L(R,r)|0j'\rangle_r\, g^L_{jj'}\,, \tag{D11$'$}$$

where $F^Q_{vj}(E_0;R)$ is the radial component of the function $\Psi_Q(E_0;R,\theta)$.

The matrices of the radial functions
$\underset{N_Q\times 1}{\mathbf{F}^Q}(E_0;R)$:=$\{F^Q_{vj}(E_0;R)\}$, $\underset{N_P\times 1}{\mathbf{f}^{P(+)}}(E;R)$:=$\{f^{P(+)}_{j'}(E;R)\}$, and
$\underset{N_P\times N^{\rm open}_P}{\mathbf{F}^{P(+)}}(E;R)$:=$\{F^{P(+)}_{j'}(E,j;R)\}$ are obtained as solutions of the following boundary value problems:

$$[E\mathbf{I}^Q{-}\mathbf{H}^{QQ}(R)]\,\mathbf{F}^Q(R) = 0\,, \tag{D14}$$
$$\mathbf{F}^Q(R_0) = \mathbf{F}^Q(R_\infty){=}0\,,$$

$$[E\mathbf{I}^P{-}\mathbf{H}^{PP}(R)]\,\mathbf{f}^{P(+)}(R) = \mathbf{H}^{PQ}(R)\,\mathbf{F}^Q(R)\,, \tag{D15}$$
$$\mathbf{f}^{P(+)}(R_0) = 0\,,\qquad \mathbf{f}^{P(+)}(R_\infty) = -\mathbf{O}^+(R_\infty)\,\mathbf{t}\,,$$

$$[E\mathbf{I}^P{-}\mathbf{H}^{PP}(R)]\,\mathbf{F}^{P(+)}(R) = 0\,, \tag{D16}$$
$$\mathbf{F}^{P(+)}(R_0) = 0\,,\qquad \mathbf{F}^{P(+)}(R_\infty) = \mathbf{O}^-(R_\infty) - \mathbf{O}^+(R_\infty)\,\mathbf{S}\,,$$

where $\mathbf{I}^s$ denote the unit matrices of dimension N^s for $s{=}P,Q$ and the symbols $\mathbf{O}^{\pm}(R)$ and $\mathbf{S}$ have the meaning described in Eq. (16) of the paper. [For $J{=}0$, $\big[\mathbf{O}^{\pm}(R)\big]_{ij}{=}\delta_{i,j}\frac{\imath}{\sqrt{2\pi\hbar}}\sqrt{\frac{\mu}{\hbar k_i}}\,\exp(\pm\imath k_i R)$ with k_i being the wave-number in the i-th open channel.]

It can be shown that the vector $\mathbf{t}$ in the boundary condition for the function $\mathbf{f}^{P(+)}(R)$ is

$$\mathbf{t} = -\imath\sqrt{2\pi}\boldsymbol{\gamma}^T \qquad \text{with} \qquad \boldsymbol{\gamma}{=}\sqrt{2\pi}\,\langle\mathbf{F}^Q\mathbf{H}^{QP}|\mathbf{F}^{P(+)}\rangle\,, \tag{D15$'$}$$

and that the following relation takes place

$$\mathrm{Im}\,\mathbf{f}^{(+)}(R) = -\sqrt{\tfrac{\pi}{2}}\,\mathbf{F}^{P(+)}(R)\,\boldsymbol{\gamma}^\dagger\,. \tag{D17}$$

The functions $\mathbf{f}^{P(+)}(R)$ and $\mathbf{F}^{P(+)}(R)$ are simply related to the functions which are directly generated in the generalized log-derivative method[11]. Namely, generated are the solutions $\boldsymbol{\Psi}^0(R)$ and $\boldsymbol{\Psi}^-(R)$ of Eq. (D15) and (D16), respectively, which satisfy the following boundary conditions: $\boldsymbol{\Psi}^0(R_0){=}\boldsymbol{\Psi}^0(R_\infty){=}0$ and $\boldsymbol{\Psi}^-(R_0){=}0\mathbf{I}^P$ and $\boldsymbol{\Psi}^-(R_\infty){=}\mathbf{I}^P$. The relations are:

$$\mathbf{f}^{P(+)}(R) \;=\; \boldsymbol{\Psi}^0(R) - \boldsymbol{\Psi}^-(R)\,\mathbf{O}^+(R_\infty)\,\mathbf{t}\,, \tag{D18}$$
$$\mathbf{F}^{P(+)}(R) \;=\; \boldsymbol{\Psi}^-(R)\,[\mathbf{O}^-(R_\infty){-}\mathbf{O}^+(R_\infty)\,\mathbf{S}]\,. \tag{D19}$$

Fig. D10. Radial components of the functions $\Phi_P^{(+)}(E;R,\theta)$ in the diabatic and adiabatic bending representations $f_{j'}^{P(+)}(E;R)$ and $f_{j'_a}^{P(+)}(E;R)$

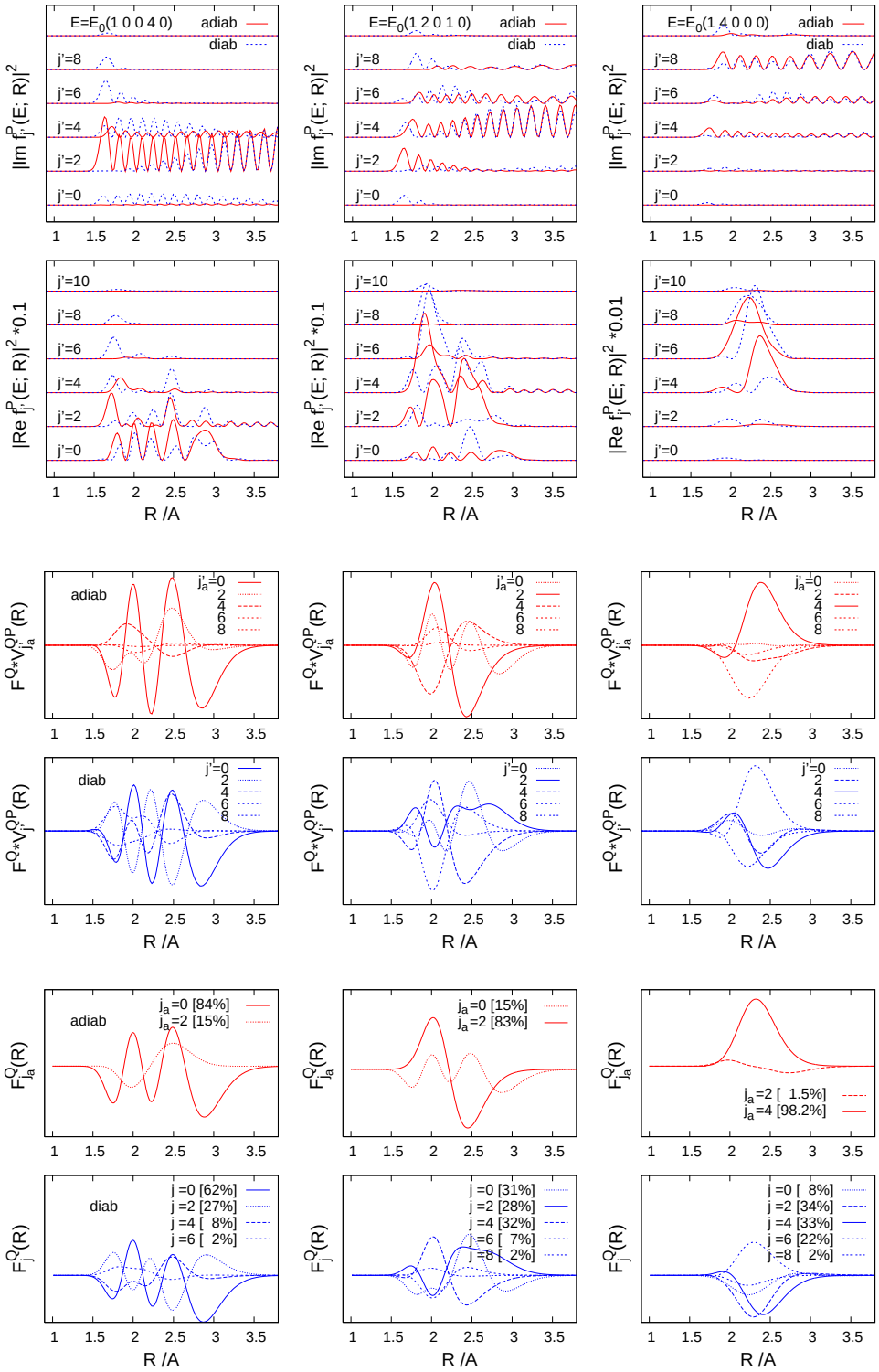

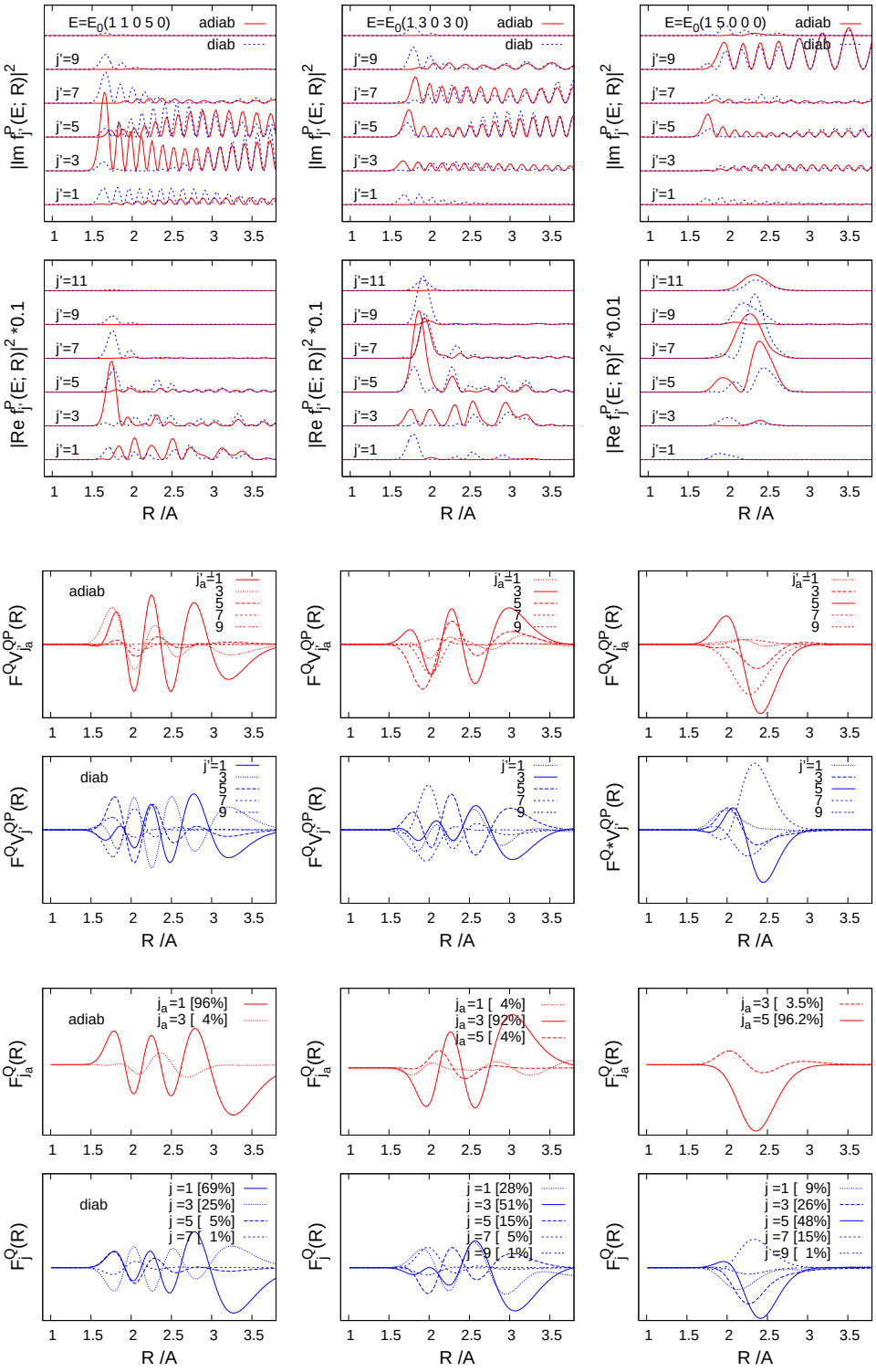

The numbers listed in the square brackets of the plots in the two lowest rows are $\rho_{1j}=\int dR\,|F^{Q}_{v=1\,j}(R)|^2\times 100\%$ and $\rho_{1j_a}=\int dR\,|F^{Q}_{v_a=1\,j_a}(R)|^2\times 100\%$. The contributions $\rho_{v>1\,j}$ and $\rho_{v_a>1\,j_a}$ to the probability integrals $\langle\Psi_Q|\Psi_Q\rangle$=1 are very small.

COMMENTS

The comparison of the respective blue and red functions in Figs. D9–D10 shows that the bending motion in the complex tends to adjust adiabatically to the changing atom-diatom distance. A consequence of this tendency in the P-subspace is the fact that the component $F^{P(+)}_{j'_a}(E,j;R)$ of the scattering function with $j'_a{=}j$ dominates not only at large R's but also in the interaction region or, at least, remains comparable there to the neighboring components $j'_a{=}j{\pm}2$. An analogous effect in the Q-subspace is the dominance of the component $F^{Q}_{j_a}(R)$ with $j_a{=}b$ (its contribution $\rho_{j_a=b}$ always much larger than the contribution $\rho_{j=b}$ of the diabatic component $F^{Q}_{j=b}$).

An important conclusion can be drawn from the upper rows of Fig. D10: for each predissociating state, the dominant component Im $f^{P(+)}_{j'_a}(R)$ of the perturbed function indicates the most populated channel of decay of the state. For states with $b{\leq}3$, it is the component with $j'_a{=}b{+}2$. Moreover, it appears that the dominant component is not fully determined by properties of the perturbing functions $F^{Q}V^{QP}_{j'_a}(R)$: the largest among these functions is always the one with $j'_a{=}b$, as seen in the third rows of the figure. Thus, the observed relations between the components Im $f^{P(+)}_{j'_a}(R)$, and the decay channel populations by the same, are all in some degree affected by transitions between the adiabatic bending states in the P-subspace.

Obviously, the impact of these non-adiabatic rotational transitions in the P-subspace becomes most substantial when the configuration regions of the largest torque are accessed, see Fig. D3. These regions are certainly accessed when the functions $|\Psi_Q(R,\theta)|$ take large values at θ's $\lesssim 45^\circ$ ($\gtrsim 135^\circ$) and R's near $2\mathring{A}$, like in the (1 4 0 0 0) and (1 5 0 0 0) cases. In these cases, the rotational transitions in the P-subspace cause the shift of the maximally populated decay channels to the highest open ones. An illustration of this fact is given in Figs. D11 and D12.

For reason given in the comment to Figs. D4–D8 the shapes of the radial components of the real parts of the perturbed functions, Re $f^{P(+)}_{j'a}(R)$, are quite different from the Im $f^{P(+)}_{j'_a}(R)$ parts. Though undoubtedly affected by interactions in the P-subspace, they remain similar to the shapes of the perturbing functions $F^{Q}V^{QP}_{j'_a}(R)$, plotted in the third rows of the figure. The shapes of the latter functions are in turn similar to the shapes of their constituents $F^{Q}_{j_a}(R)$ with $j_a{=}j'_a{=}b$, plotted in the fifth rows. A difference should be noted, however, in cases with excited bending vibrations ($b{-}k{>}0$): an additional oscillation occurs in the functions $F^{Q}V^{QP}_{j'_a=b}(R)$ at small R side. It comes from the V^{QP} coupling, from the change of sign along the red line shown in the right upper panel of Fig. D3. [The feature is even better seen in the 2D plots of $\Psi_Q H_{QP}$ in Fig. D4a, the (1 5 0 0 0) case].

The extra oscillation in the perturbing functions produced by the V^{QP} coupling can certainly have a role in determining the widths Γ of states with excited bending mode. Namely, it can act towards lessening of these widths as compared to the widths of states tightly localized around $\theta{=}\pi/2$. This explains in part the v_θ-dependence of the total VP widths described in the paper.

Fig. D11. Level shifts, partial and total widths as functions of R- coordinate

$$E^{\rm shft}(R) = {\rm Re}\sum_{j'_a} F^Q V^{QP}_{j'_a}(R)\, f^{P(+)}_{j'_a}(R)$$

$$\Gamma(R) = -2{\rm Im}\sum_{j'_a} F^Q V^{QP}_{j'_a}(R)\, f^{P(+)}_{j'_a}(R) \quad \left[=\sum_{j'_a}\Gamma_{j'_a}(R)\right]$$

$$\Gamma_j(R) = \gamma_j(R)\,\gamma^*_j = \sum_{j'_a}\Gamma_{j'_a\,j}(R)\,, \qquad \Gamma_{j'_a\,j}(R) = \gamma_{j'_a\,j}(R)\,\gamma^*_j$$

$$\gamma_j(R) = \sqrt{2\pi}\sum_{j'_a} F^Q V^{QP}_{j'_a}(R)\, F^{P(+)}_{j'_a}(E_0, j; R) = \sum_{j'_a}\gamma_{j'_a\,j}(R)$$

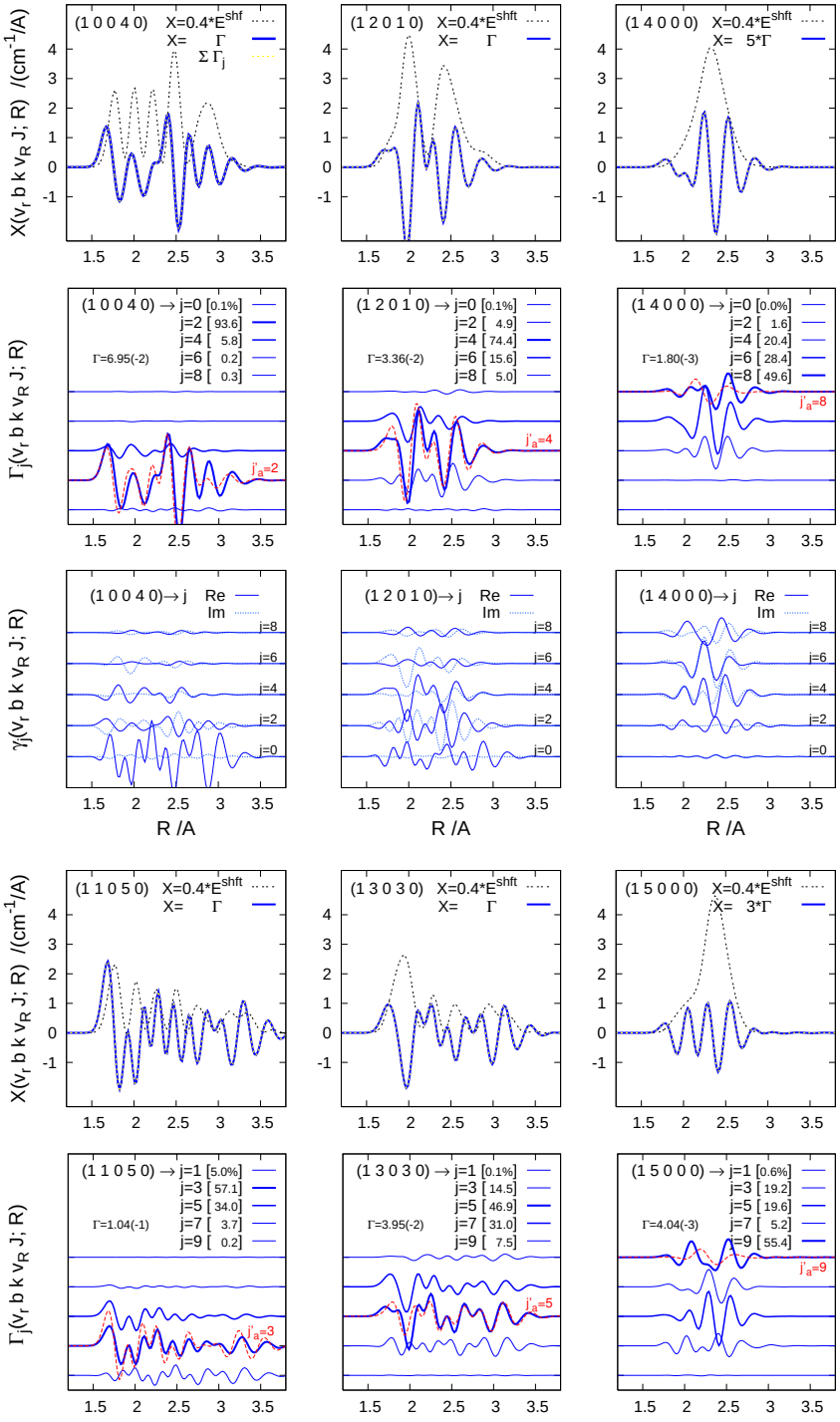

The numbers in the square brackets in the legends of the plots of Γ_j, here and in Fig. D12, are the populations $\Gamma_j/\Gamma\times 100\%$ of the decay channels D(v=0, j)+Li$^+$ of the (v_r=1 b k=0 v_R J=0) states shown.

Fig. D12. Level shifts, partial and total widths as functions of θ- coordinate

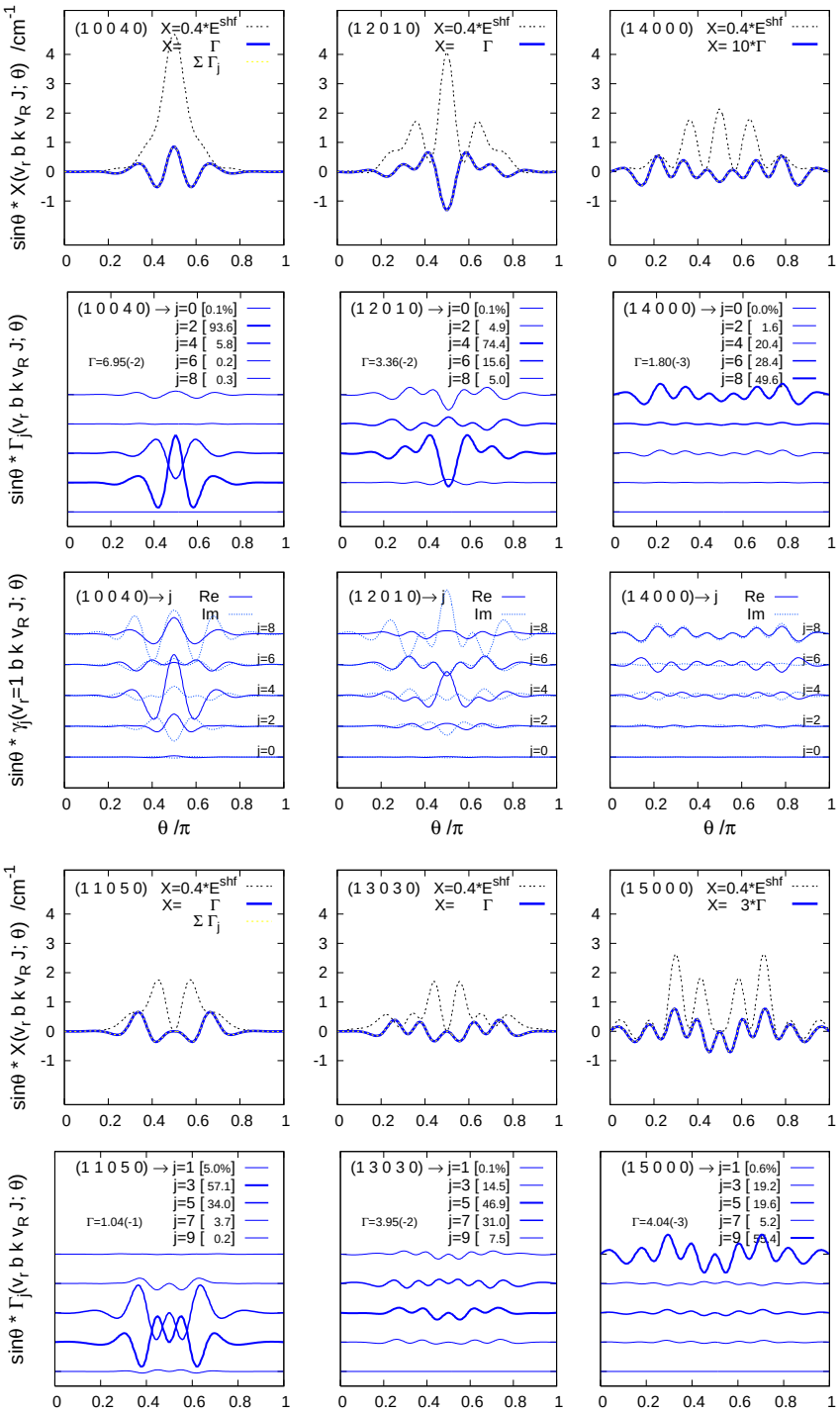

It is to note in Figs. D11 and D12 that the most populated channel j (the largest Γ_j) for a given predissociating state is indicated by the magnitude (of oscillations) of the corresponding function $\Gamma_j(R)$ and/or $\Gamma_j(\theta)$. The decay amplitude functions $\gamma_j(R)$ and $\gamma_j(\theta)$ show usually quite different relations, as e.g. in the (1 0 0 4 0) and (1 2 0 1 0) cases. Therefore, one cannot relay on inspection of these functions in the analysis of the predissociation dynamics.

The components $\Gamma_{j'_a\,j}(R)$ with $j'_a{=}j$ of the largest partial widths Γ_j, shown in Fig. D11 (red curves), reproduce rather closely the entire functions $\Gamma_j(R)$. Substantial differences occur, however, in the (1 4 0 0 0) and (1 5 0 0 0) cases. The integrated contributions $\Gamma_{8\,8}$ and $\Gamma_{9\,9}$ to the widths $\Gamma_{j=8}$ and $\Gamma_{j=9}$, respectively, are even negative and other components $\Gamma_{j'_a\,j}$, with $j'_a{<}j$, bring even more substantial positive contributions. This is another evidence of the increased role played in these cases by the rotationally non-adiabatic transitions in the P-subspace; see the comments below Fig. D10.

Fig. D13. Vibrational predissociation widths of J-levels in different groups $[v_r{=}1\, v_\theta\, v_R]\, k$

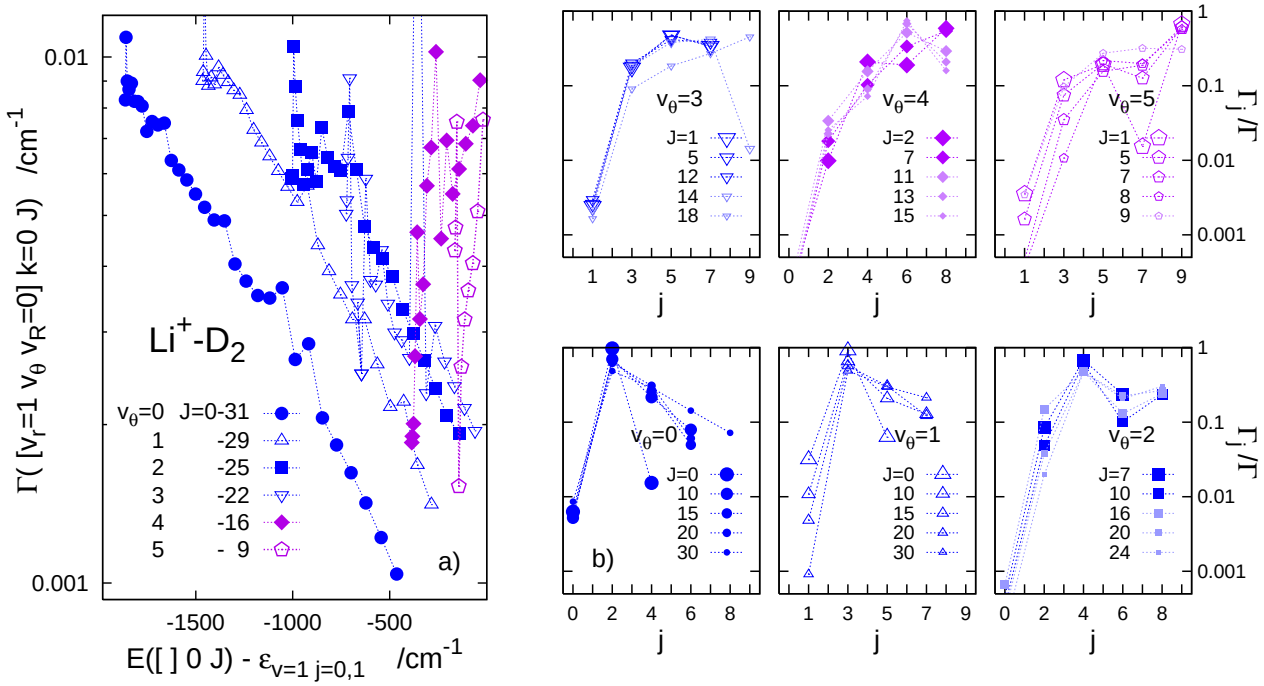

D13a. Total widths of J-levels in $k{=}0$ groups of $[1\, v_\theta\, 0]$ states with $v_\theta{=}0{-}5$ shown as functions of 'binding' energy which is defined here as $E([1\, v_\theta\, 0]\, 0\, J){-}\varepsilon_{v=1\, j}$ with $j{=}0$ for $v_\theta{=}0, 2, 4$ and $j{=}1$ for $v_\theta{=}1, 3, 5$.

D13b. Populations of $Li^+ + D_2(v{=}0\, j)$ channels due to VP of selected J-levels in groups $[1\, v_\theta\, 0]\, k{=}0$ for $v_\theta{=}0{-}5$.

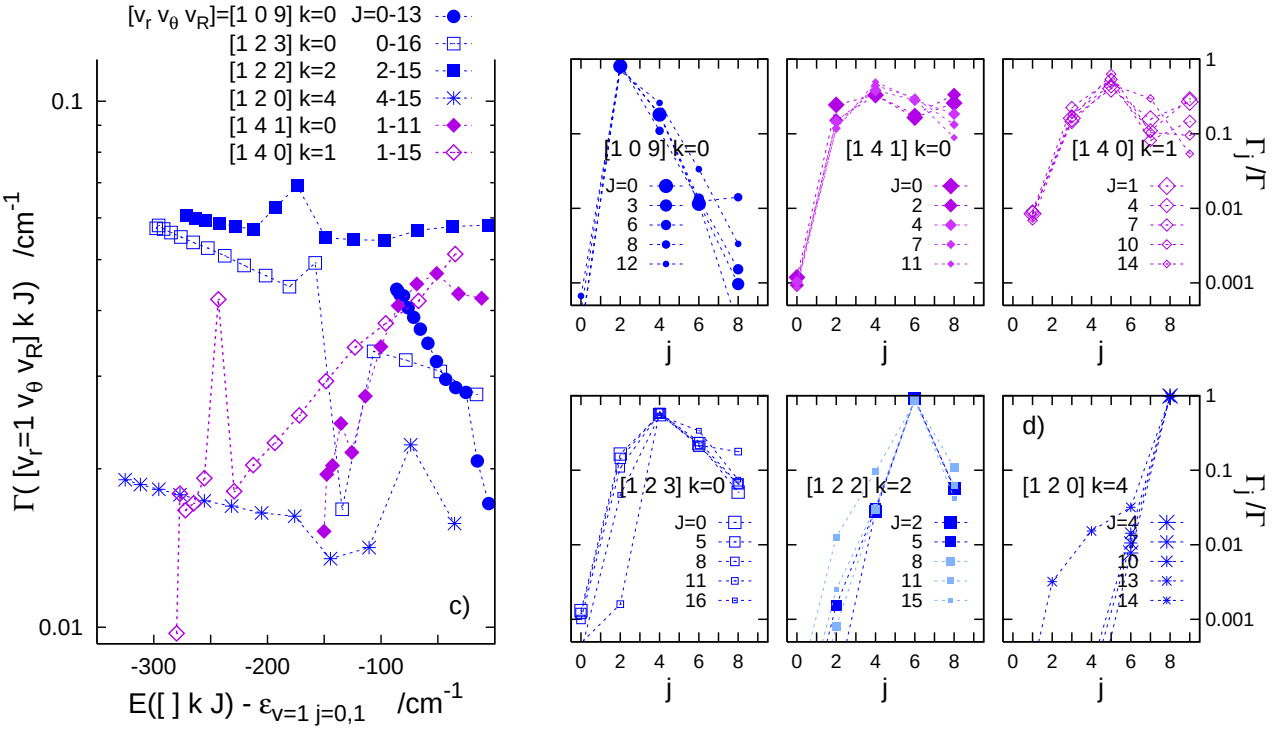

D13c and **D13d** — same as in panels D13a and D13b, respectively, but for J-levels in groups $[v_r{=}1\, v_\theta\, v_R]\, k$ with $v_R{>}0$ and/or $k{>}0$.

COMMENTS

The purpose of Fig. D13a is to display how the VP widths behave upon the increase of centrifugal barriers (J-number) in states with excited bending vibrations. A dramatic change in this behavior occurs in the two highest excited states shown, v_θ=4 and v_θ=5. At low J's, the widths in the violet curves, especially in the v_θ=4 curve, are much smaller than one would expect from the values in the v_θ=2−3 curves at J's in the same 'binding' energy region. The decay of the complex from its high v_θ–low J-states is substantially affected by the anisotropic interactions in the final, continuum-state, subspace; see the comments below Fig. D10. By driving transitions to the highest accessible j-channel in this subspace the interactions apparently slow down the decay process. With growing J, the increasing centrifugal barriers [together with the increasing energy release, $E([\ ]kJ)-\varepsilon_{00}$, cause a gradual weakening of the effective anisotropy; the decay becomes thus less and less retarded. Such explanation may be offered for the rapid growth of the violet curves.

The populations curves shown in the v_θ=4 and v_θ=5 panels of Fig. D13b seem to support this explanation. The curves pertaining to low J's (darker) are indeed peaked at the highest accessible channels j=8 and j=9. For larger J's, however, the peaks shift down; they occur at j=6 in all J>7 curves in the v_θ=4 panel.

The comparison of the curves from Fig. D13a with the corresponding population curves in Fig. 13b suggest that there is a correlation between the decrease (increase) of the total VP widths with growing J and the feature of the partial widths to have (not to have) a maximum at j=v_θ+k+2.

Figs. D13c–d provide some evidence that the described tendencies among the total and partial VP widths of different J-levels are not limited to levels in the groups $[1\,v_\theta\,0]\,k$=0 but may show up also in groups with v_R>0 and/or k>0. In Fig. D13c, a qualitative difference in the behavior of the total widths with growing J is seen between the groups $[1\,4\,1]\,0$ and $[1\,4\,0]\,1$ on one side and the groups $[1\,0\,9]\,0$, $[1\,2\,3]\,0$, $[1\,2\,2]\,2$ and $[1\,2\,0]\,4$ on the other side. Like in Fig. D13a, the discriminating factor is the degree of excitement of bending vibrations: $v_\theta\geq$4 versus $v_\theta\leq$2. In Fig. D13d, clear maxima at j=v_θ+k+2 are displayed by all curves that represent populations of j-channels due to decay of the selected states with $v_\theta\leq$2 (drawn in blue). In the decay of the v_θ=4 states, in turn, this rule is not obeyed: maxima at j=5 occur in the curves for $[1\,4\,0]\,1\,J$ levels and two weak maxima, at j=4 and j=8, in the curves for $[1\,4\,1]\,0\,J$ levels.

$\mathbf{Li^+}$–$\mathbf{D}_2$ versus $\mathbf{Li^+}$–$\mathbf{H}_2$

Fig. D14. Energies and widths of $[v_r\, v_\theta{=}0\, v_R]$ $J{=}0$ states

D14a. $E^{\rm shft}$ and Γ as functions of R- coordinate

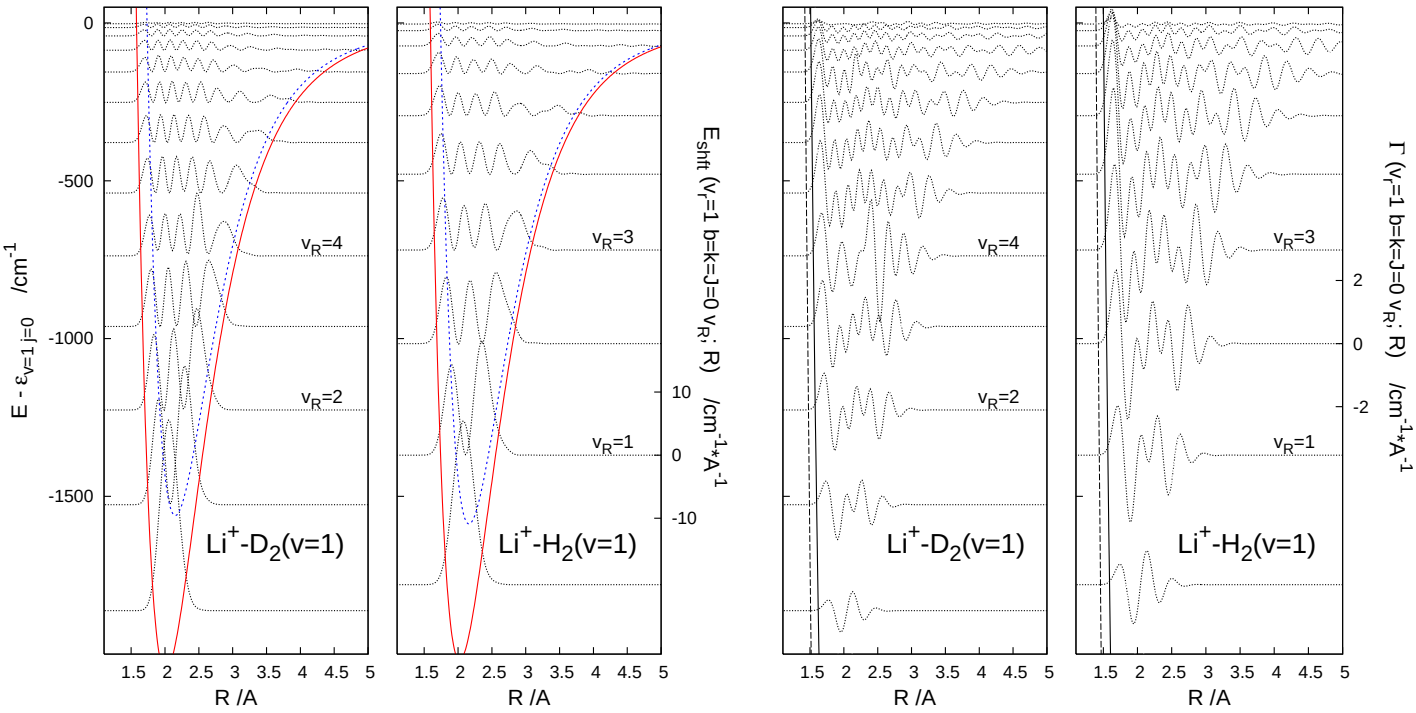

The functions $E^{\rm shft}(R)$ and $\Gamma(R)$ are the gray dotted curves with the wavy parts. The ordinate values of baselines of these curves indicated on the left-hand axes are the energies of the states relative to the $v{=}1\, j{=}0$ threshold. The blue dotted curves are the diabatic potentials $W^{Q}_{v=1j=0;1\,0}(R)$ and the red curves are the lowest adiabatic potentials $e^{Q}_{v_a=1\, j_a=0}(R)$ in the Q-subspaces of the complexes. The P- and Q-subspaces for the $\rm Li^+$–$\rm H_2$ complex are defined analogously to the subspaces for $\rm Li^+$–$\rm D_2$, see Fig. D3. The near vertical lines in the right-hand panels are parts of the adiabatic potentials in the P-subspaces, $e^{P}_{v'_a=0\, j'_a=0}(R)$ (dashed) and $e^{P}_{0\, j'_a=2}(R)$.

D14b. Analysis of $\Gamma([1\,0\,0]J{=}0; R)$

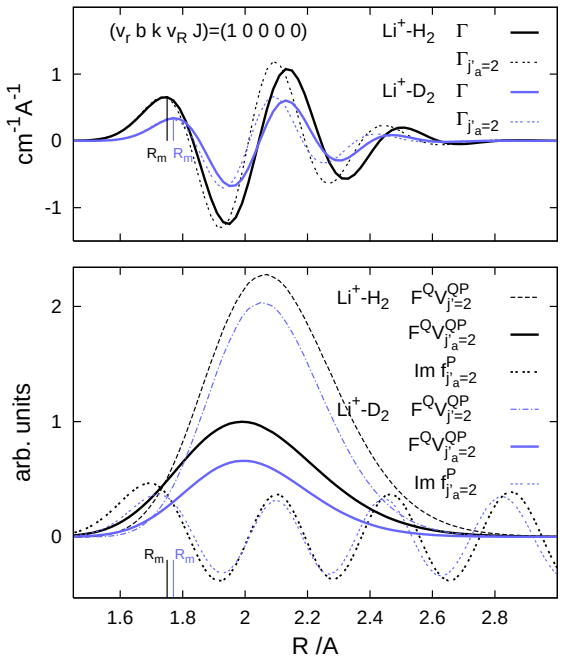

Upper panel: Total width functions $\Gamma(R)$ of the $[1\,0\,0]J{=}0$ state of the two complexes and their largest components $\Gamma_{j'_a}(R)$, with $j'_a{=}b{+}2{=}2$. j'_a is the quantum number of the adiabatic bending state in the P-subspace. See Fig. D11, where the resolution $\Gamma(R){=}\sum_{j'_a}\Gamma_{j'_a}(R)$ is defined.

Lower panel: A comparison of the functions $\Gamma_{j'_a=2}(R)$ for the two complexes,

$$\Gamma_{j'_a}(R) = -2F^{Q}V^{QP}_{j'_a}(R) \times {\rm Im}f^{P(+)}_{j'_a}(R)\,.$$

Compared are separately the two constituents of the functions, $F^{Q}V^{QP}_{j'_a=2}(R)$ and ${\rm Im}f^{P(+)}_{j'_a=2}(R)$; see Eqs. D11–D11' and D15–D17 for their definitions. The largest difference is revealed by the first constituent. The ratio of the value of $F^{Q}V^{QP}_{j'_a=2}(R{=}R_m)$ for $\rm Li^+{-}H_2$ to the value for $\rm Li^+$–$\rm D_2$ (at the blue R_m) is close to the ratio of the reduced masses: $\mu_{\rm Li^+-D_2}/\mu_{\rm Li^+-H_2}$. The ratio of the respective values of the function ${\rm Im}f^{P(+)}_{j'_a}(R)$ appears close to $\mu^{-1/4}_{\rm H_2}/\mu^{-1/4}_{\rm D_2}$.

D14c. Scaling properties of $E^{\rm shft}$ and Γ of $[v_r{=}1{-}3\ v_\theta{=}0\ v_R]\ J{=}0$ states

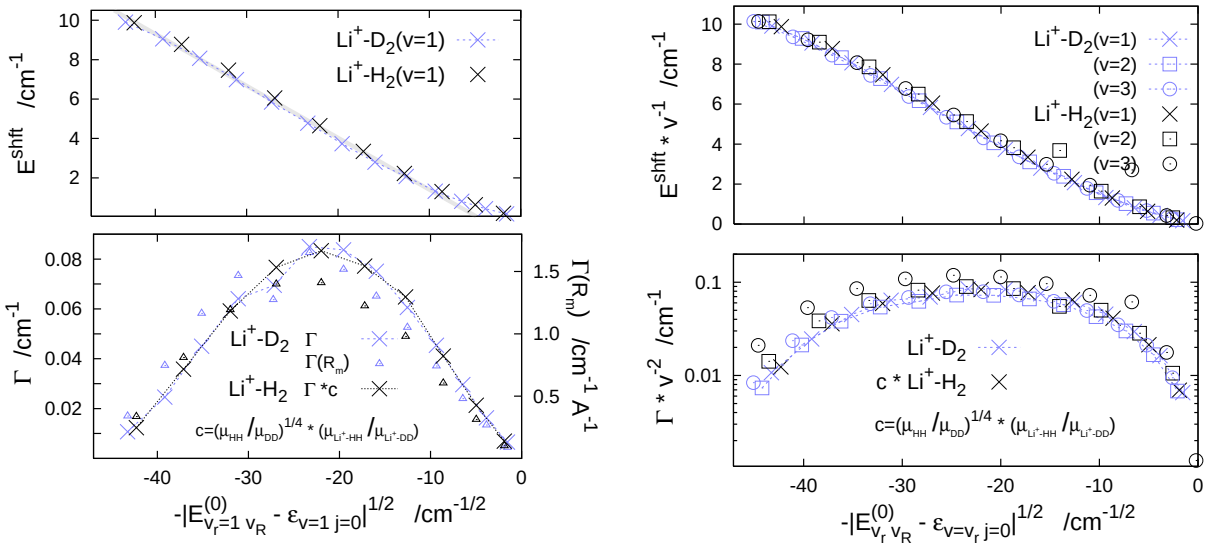

$E^{(0)}_{v_r\,v_R}$ — 0-th order approximation to energy of a given $[v_r\,0\,v_R]\ J{=}0$ state, i.e. the energy of corresponding state in the Q-subspace containing three closed v-channels, $v{=}v_r, v_r{+}1, v_r{+}2$. $\varepsilon_{v=v_r\ j=0} - E^{(0)}_{v_r\,v_R}$ — binding energy in the Q-subspace. c — scaling factor deduced from inspection of the width functions $\Gamma(R)$ in Fig. D14b. $\Gamma(R_m)$ — the value of the width function of a given $[1\,0\,v_R]\ J{=}0$ state at position of the first maximum $R_m{\approx}1.6{-}1.7\mathring{A}$, as shown in Fig. D14a (in the two right-hand panels).

COMMENTS

The properties illustrated in Fig. **D14c** are:

(i) The shifts $E^{\rm shft}$ of the $E^{(0)}_{v_r\,v_R}$ levels in the two complexes depend only on the binding energy $|E^{(0)}_{v_r\,v_R} - \varepsilon_{v=v_r\ j=0}|$, denoted in the following comments shortly as B^Q.

(ii) The shifts decrease with decreasing $\sqrt{B^Q}$ approximately linearly, except for the region of B^Q's smaller than $\sim$100 cm^{-1}.

(iii) The $E^{\rm shft}$s grow approximately linearly with increasing vibrational excitation of the diatomic subunit, at least, in the range of low v.

(iv) The widths Γ of the states $[v_r\,0\,v_R]\ J{=}0$ with fixed v_r show a Gaussian-like dependence on $\sqrt{B^Q}$. The dependence is qualitatively indicated by the heights of the maxima in the widths functions $\Gamma(R)$ near the classical turning points in the respective P-subspaces.

(v) The curve $\Gamma(\sqrt{B^Q})$ for Li$^+$–H$_2$($v{=}1$), when multiplied by the mass factor c defined in the figure ($c{=}0.51449$), coincides almost perfectly with the respective curve for Li$^+$–D$_2$($v{=}1$).

(vi) The curves $\Gamma(\sqrt{B^Q})$ that pertain to states of the Li$^+$–D$_2$(v) complex are, apart from the multiplicative factor of v^2, practically the same for the three lowest v's. Larger differences occur between the curves pertaining to Li$^+$–H$_2$(v) for $v{=}1,2$ and for $v{=}3$, especially between their low-v_R parts (the Γ's are listed in Table IX).

Li^+–D_2 versus Li^+–H_2

Fig. D15. Widths of $[v_r{=}1\ v_\theta\ v_R]\ k{=}J$ states

Correlation with binding energy in the Q-subspace

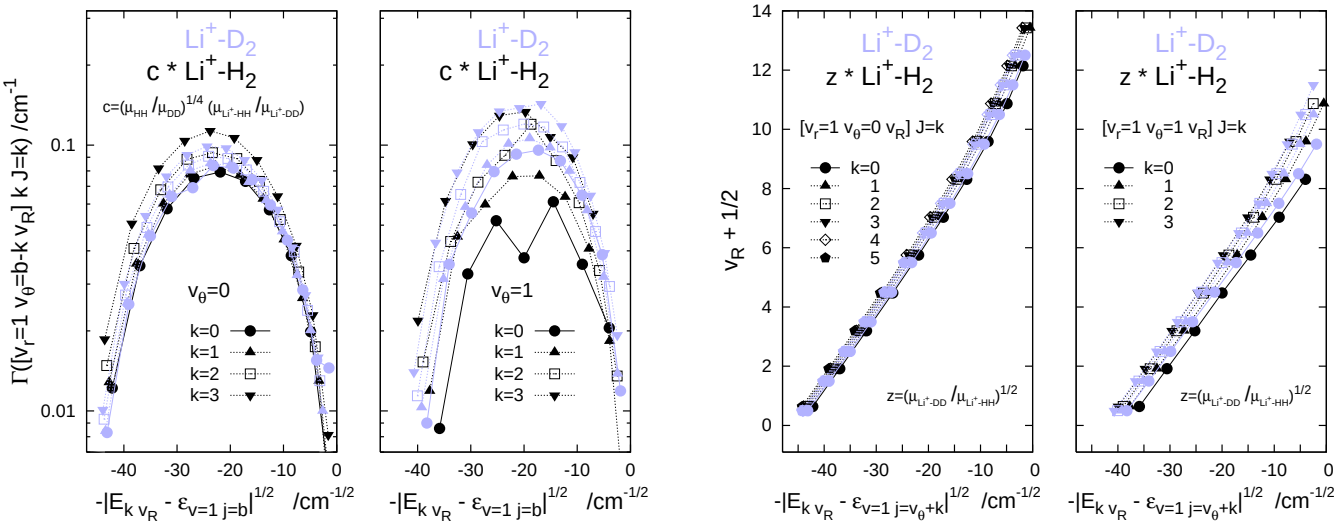

D15a. Most of the widths shown in Fig. 8 of the paper as functions of the number v_R are re-plotted here as functions of (minus) square-root of the binding energy of the states relative to their respective threshold in the closed-channel (Q) subspace. After the re-plotting, the k=0−2-curves formed of the widths of the two complexes in the states with v_θ=0 appear to differ merely by a multiplicative factor, approximately equal to the c defined in Fig. D14. In the right panel, the k=0, 1-curves formed of the widths $\Gamma^{\mathrm{Li^+-aa}}([v_r{=}1\ v_\theta{=}1\ v_R]k\ J{=}k)$ for a=H exhibit substantial distortions. Therefore these curves cannot be made close to their counterparts for a=D by the simple mass-scaling.

D15b. The numbers $v_R{+}\frac{1}{2}$ of the states considered appear to depend nearly linearly on square-root of the binding energies of the states. The blue and black symbols used for a given k would lie on exactly the same perfectly straight line if the R-motion in the corresponding states of the two complexes were effectively governed by the same Morse-type potential.

The functions $\Gamma(v_R;k)$ plotted in panels a) and b) of Fig. 8 in the paper, when superposed with the functions plotted here, give the functions shown in panel d) of Fig. 8 and in Fig. D15a here (without the factors c, of course).

D15c. The widths due to vibrational predissociation of the Li^+–D_2 complex shown in the two panels of Fig. D15a, for states with v_θ=0, 1, are compared here with their counterparts for states with higher excited bending vibrations, v_θ=2–5.

For each v_θ, the dark-blue symbols show the widths for different v_R and k=0, the lighter and smaller symbols are used for other k-values from the range listed in the legend.

The decrease of the widths with growing v_θ shown in Fig. 10c (by the arrows) on the levels $[v_r{=}1\ v_\theta\ v_R{=}0]\ J{=}0$ is demonstrated here to occur also among $J{=}k$ levels of a number of states excited additionally in the R-mode.

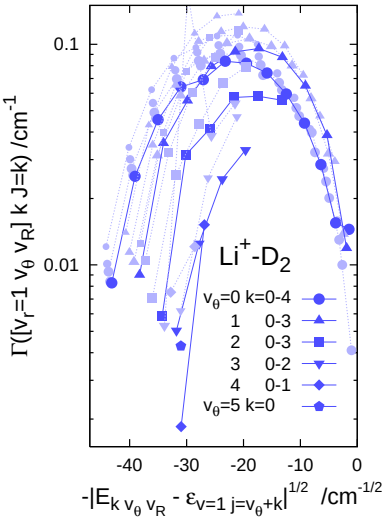

$Li^+–D_2$ versus $Li^+–H_2$

Fig. D16. Widths of $[v_r{=}1, 2\, v_\theta{=}0\, v_R{=}0]\, k\, J$ states

Correlations with binding energy in the Q-subspace and ....

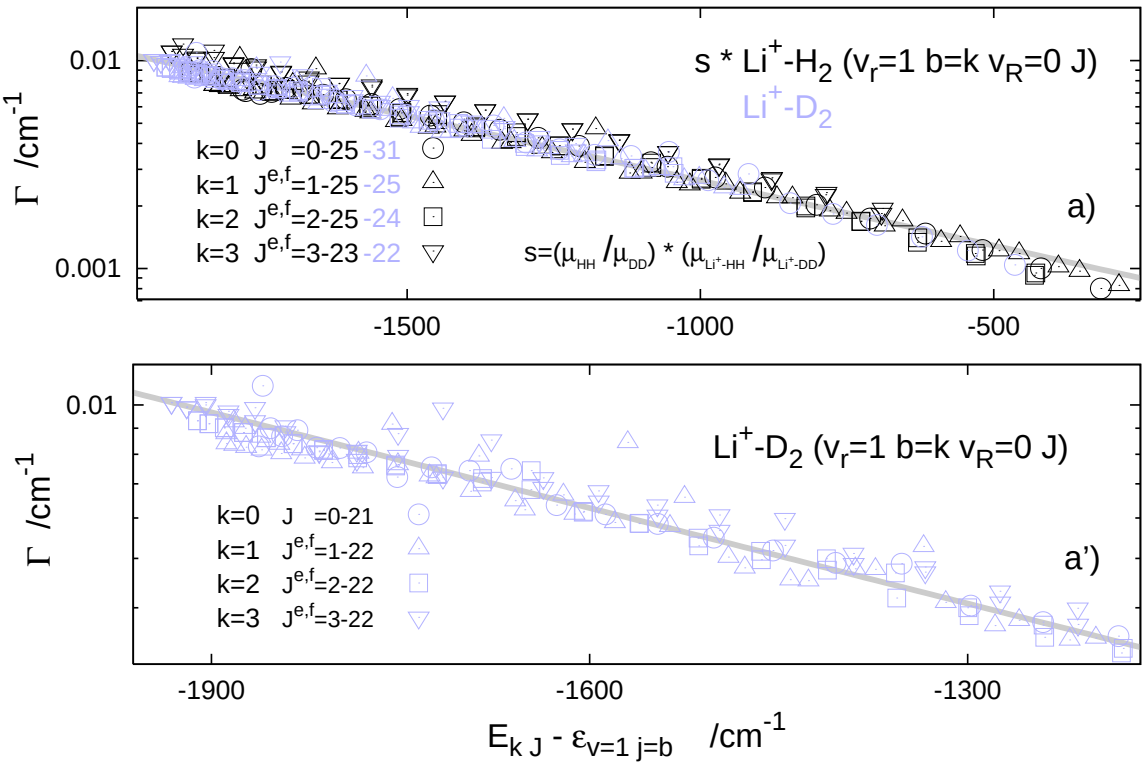

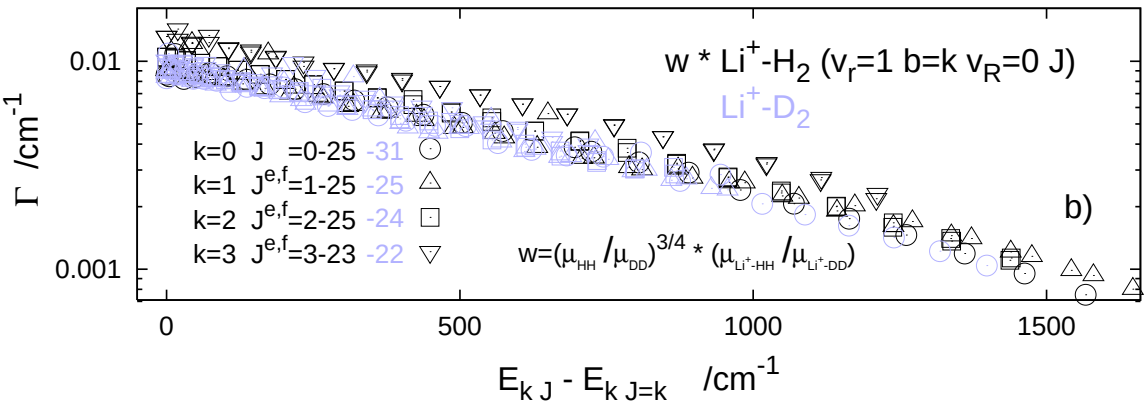

$\sim v_r^2$ -dependence

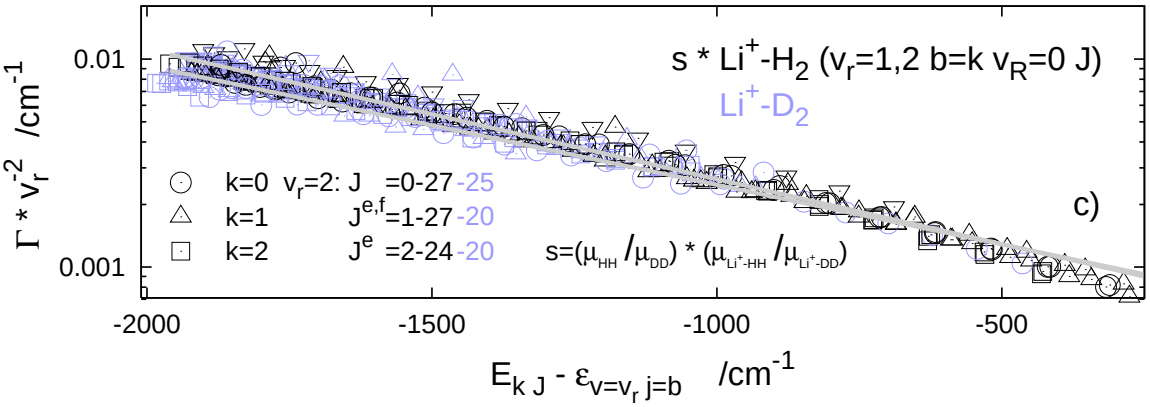

The J levels of $v_r{=}1$ state shown here, not listed in the legend, are the same as shown in panel a).

... momentum of translational (R) motion in the P-subspace

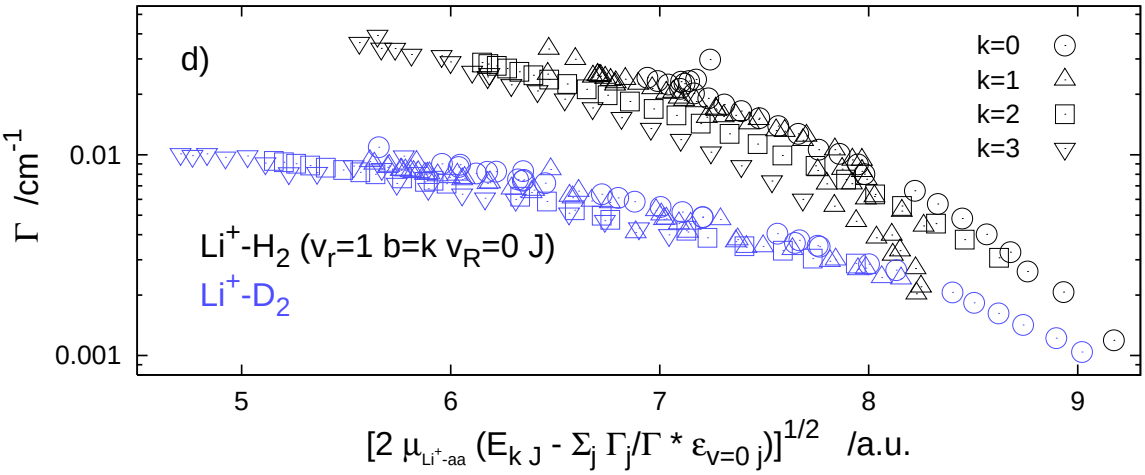

COMMENTS

The set of widths shown in panel a) of Fig. D16 is the same as shown in Fig. 9 of the paper. It appears that all the widths in the set, excluding the most strongly disturbed ones, can roughly be described with the formula [plotted with gray line in panels a) and a')]

$$\Gamma_{kJ}^{\mathrm{Li}^+-\mathrm{aa}} = 1/s^{\mathrm{a}}\,\exp[\alpha-\beta(E^{\mathrm{a}}_{kJ}-\varepsilon^{\mathrm{a}}_{v=v_r\,j=k})] \qquad \text{for a=H,D}\,, \tag{D20}$$

where $s^{\mathrm{a}}=\frac{\mu_{\mathrm{aa}}}{\mu_{\mathrm{DD}}}\,\frac{\mu_{\mathrm{Li}^+-\mathrm{aa}}}{\mu_{\mathrm{Li}^+-\mathrm{DD}}}$ (s^{H}=0.3060), $E^{\mathrm{a}}_{kJ}-\varepsilon^{\mathrm{a}}_{v_r\,k}$ is the 'binding' energy of the Li^+-aa complex in a given $[v_r\,0\,0]\,k\,J$ state (if it would never decay), and α and β are parameters; their values (for v_r=1 here) are -7.374 ln(cm^{-1}) and 0.001440 1/cm^{-1}, respectively.

The features of the VP widths displayed in panels a) and a') occur also in some higher excited vibrational states of the Li^+–$\mathrm{H}_2(\mathrm{D}_2)$ complexes. More precisely, they are likely to occur in states with higher excited diatomic and atom-diatom stretching vibrations, as indicated by the [2 0 0], [1 0 1], and [1 0 2] cases in Fig. 9 of the paper, but rather not in states with excited atom-diatom bending, as indicated in Fig. D16' below. An explanation of the latter fact may be the observation that the rotational levels of the particular k groups of $v_\theta>0$ states are more susceptible to perturbations when crossing with levels from other groups/states.

In panel b) of Fig. D16, the widths are plotted as functions of the rotational energy $E_{k\,J}-E_{k\,J=k}$. This option is mentioned in the paper, in the comments on Fig. 9. The main effect is indeed the same as presented in panel a): the widths of $k\,J$-levels of both complexes form nearly parallel lines. The difference concern the factors which are needed to make the lines nearly overlapping. The factor w used for this goal in panel b) works as good as the factor s used in panel a). However, tests have shown the w does not (or would have to be modified in order to) reflect equally well the relations between the $k\,J$-level widths of the two complexes as functions of the energy $E_{k\,J}-E_{k\,J=k}$ in the excited vibrational states, even in the three mentioned above: [2 0 0], [1 0 1], and [1 0 2].

In panel c) of Fig. D16, the sets of widths of ($k\,J$) levels of the complexes Li^+–$\mathrm{H}_2(\mathrm{D}_2)$ in their states [1 0 0] and [2 0 0] are re-plotted in a way exposing the near-quadratic dependence on the number v_r. The two nearly-coincident gray lines represent fits of the widths in the two states to formula (D20). The parameters obtained for $\frac{1}{(v_r=2)^2}\Gamma_{kJ}^{\mathrm{Li}^+-\mathrm{aa}}([2\,0\,0])$ are: $\alpha=-7.318$ ln(cm^{-1}) and β=0.001320 1/cm^{-1}.

In panel d) of Fig. D16, it is demonstrated that the decrease of the widths with growing J and the increase for a given $J>3$ with k growing from 0 to 3 (both effects seen in Fig. 9) can be explained for each complex by the momentum gap law[12]. The energy of relative translational motion of the fragments in the v=0 channel is obtained by substraction from the total energy released in the decay of state $[1\,0\,0]k\,J$) the part which is transferred to rotations of the diatom. This part is estimated using the calculated j-state populations $P_j=\Gamma_j/\Gamma$.

Fig. D16'. Widths of $[v_r{=}1\, v_\theta{=}1{-}2\, v_R{=}0]\, k\, J$ states

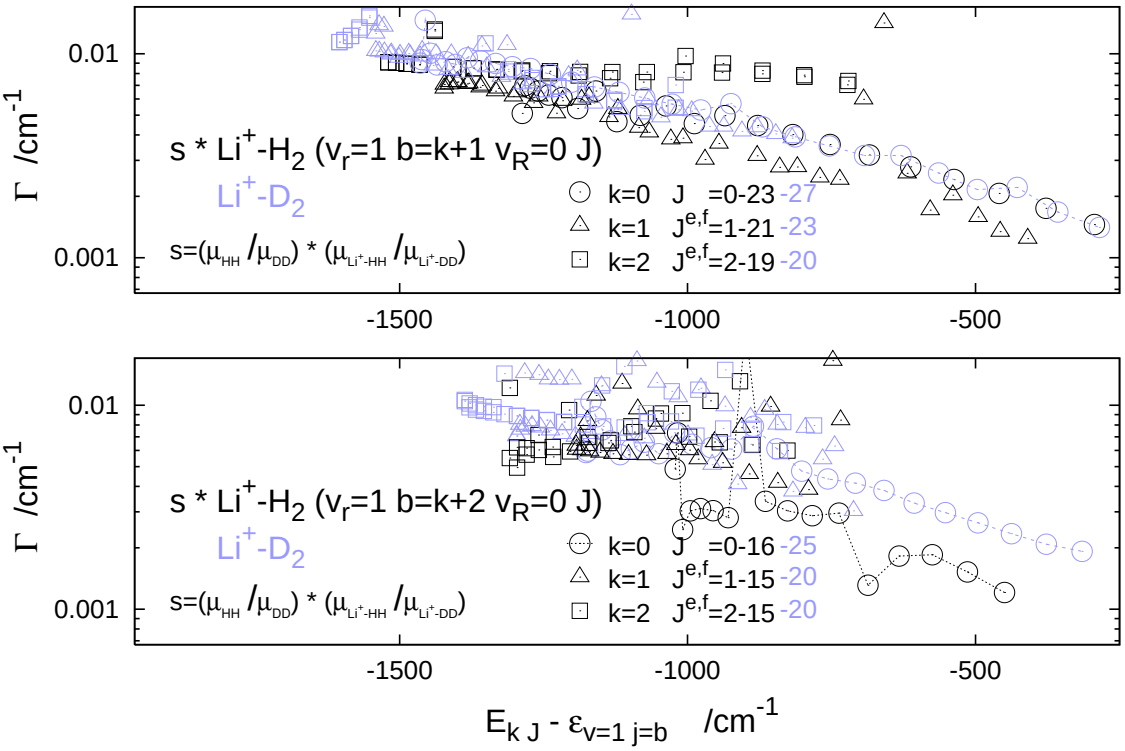

---

[1] O. K. Rice, J. Chem. Phys. **1**, 375 (1933); U. Fano, Phys. Rev. **124**, 1866 (1961); J. N. Bardsley, J. Phys. **B1**, 349 (1968); F. H. Mies, Phys. Rev. **175**, 164 (1968).

[2] F. T. Smith, Phys. Rev. **118**, 349 (1960).

[3] F. Mrugała and R. Moszynski, J. Chem. Phys. **109**, 10823 (1998); Part A of this material.

[4] N. Halberstadt, J. A. Beswick, and K. C. Janda, J. Chem. Phys. **87**, 3966 (1987).

[5] O. Roncero, J. A. Beswick, N. Halberstadt, P. Villareal, and G. Delgado-Barrio, J. Chem. Phys. **92**, 3348 (1990).

[6] C. Sanz, E. Bodo, and F. A. Gianturco, Chem. Phys. **314**, 135 (2005).

[7] part B of this material.

[8] F. Mrugała and W. P. Kraemer, J. Chem. Phys. **122**, 224321 (2005).

[9] Part C of this material.

[10] R. Schinke, *Photodissociation Dynamics*, Cambridge Univ. Press, Cambridge 1993.

[11] F. Mrugała, Int. Rev. Phys. Chem. **12**, 1 (1993).

[12] G. E. Ewing, J. Chem. Chem. **71**, 3143 (1979).